Synchrotron infrared nano-spectroscopy and -imaging

Hans A. Bechtel [a, *], Samuel C. Johnson [b], Omar Khatib [a, b], Eric A. Muller [b],
Markus B. Raschke [b, **]

[a] *Advanced Light Source Division, Lawrence Berkeley National Laboratory, Berkeley, CA 94720, USA*
[b] *Department of Physics, Department of Chemistry, and JILA, University of Colorado, Boulder, CO 80309, USA*

ARTICLE INFO

ABSTRACT

Infrared (IR) spectroscopy has evolved into a powerful analytical technique to probe molecular and lattice vibrations, low-energy electronic excitations and correlations, and related collective surface plasmon, phonon, or other polaritonic resonances. In combination with scanning probe microscopy, near-field infrared nano-spectroscopy and -imaging techniques have recently emerged as a frontier in imaging science, enabling the study of complex heterogeneous materials with simultaneous nanoscale spatial resolution and chemical and quantum state spectroscopic specificity. Here, we describe synchrotron infrared nano-spectroscopy (SINS), which takes advantage of the low-noise, broadband, high spectral irradiance, and coherence of synchrotron infrared radiation for near-field infrared measurements across the mid- to far-infrared with nanometer spatial resolution. This powerful combination provides a qualitatively new form of broadband spatio-spectral analysis of nanoscale, mesoscale, and surface phenomena that were previously difficult to study with IR techniques, or even any form of micro-spectroscopy in general. We review the development of SINS, describe its technical implementations, and highlight selected examples representative of the rapidly growing range of applications in physics, chemistry, biology, materials science, geology, and atmospheric and space sciences.

© 2020 Elsevier B.V. All rights reserved.

Contents

* Corresponding author.
** Corresponding author.
  E-mail addresses: habechtel@lbl.gov (H.A. Bechtel), markus.raschke@colorado.edu (M.B. Raschke).

1. Introduction

The development of imaging techniques that provide chemical or quantum state information with simultaneous spatial resolution on the nanometer scale with large fields of view is critical for understanding the compositional, structural, and functional interactions of many natural and engineered systems. For example, the elementary processes of life, such as respiration and photosynthesis, occur on multiscale (molecular to mesoscopic) dimensions and rely on the exchange of molecules between cells and their environment. Similarly, molecular materials gain their functional properties from their local arrangement and inter-molecular interactions that give their defining electronic, charge transport, interfacial, or chemical characteristics. Lastly, the atomic and nanoscale heterogeneity of quantum materials defines macroscopic catalytic, magnetic, electronic, photonic, and phononic properties through the control of composition, structure, spin, band gaps, and electron transport.

Infrared spectroscopy has long been established as a routine analytical technique capable of chemical identification and structural determination [1]. Based on absorption by infrared-active vibrational and phonon modes, this label-free and minimally invasive technique is broadly applicable to a wide range of scientific disciplines, including biology, chemistry, energy science, geology, condensed matter physics, and space sciences. As a form of vibrational spectroscopy, many applications of infrared spectroscopy rely on monitoring the behavior of strong diagnostic bands or functional groups that occur at characteristic frequencies (Fig. 1). Other applications use infrared light to probe Drude conductivity and low-energy excitations, such as band gaps, plasmons, and excitons.

The combination of infrared spectroscopy with conventional microscopy has enabled chemical analysis and imaging at the micrometer scale [3,4]. Infrared microscopes have conventionally achieved the best spatial resolution by using reflective Schwarzschild objectives in combination with apertures in a confocal geometry [5]. The spatial resolution is limited by diffraction to typically 2–20 μm in the mid-IR (500-4000 cm^{-1}) using standard objectives with numerical apertures (NA) ~0.50. Recently, the development of commercial infrared focal plane array (FPA) detectors has enabled rapid acquisition of chemical images with fields of view greater than 100×100 μm^2. Although the imaged pixel size of FPA detectors can be less than 1×1 μm^2, the spatial resolution remains limited by diffraction, and can only be marginally improved beyond the Abbe limit through oversampling and point spread function deconvolution techniques [6–8].

To systematically reach beyond the conventional far-field diffraction limit, near-field microscopy in principle provides diffraction unlimited spatial resolution. Near-field scanning optical microscopy (NSOM) typically relies on raster scanning an aperture of sub-diffraction size d, e.g., based on a tapered optical fiber probe, manipulated close to the sample surface within the spatial extent of the evanescent near-field of the aperture [9–12]. The spatial resolution is then no longer determined by the wavelength λ of light, but extrinsically given by the dimension of the aperture. While this approach provides spatial resolution higher than the conventional far-field diffraction limit and is independent of wavelength, reaching into the nanometer regime, the extension of NSOM beyond the visible into the infrared spectral range has been limited by the availability of IR transparent fiber materials and severe attenuation at extended wavelengths due to the waveguide cut-off effect. Furthermore, the sensitivity is limited by the collection efficiency due to near-field aperture transmission scaling as $(d/\lambda)^4$ for typical circular apertures [13,14]. This scaling factor is particularly detrimental with increasing wavelengths, making infrared measurements with nanometer spatial resolution very difficult in practice.

To overcome these constraints, alternative near-field techniques have been developed that use external illumination of a metallic or metallized scanning probe tip rather than relying on near-field localization by a tapered optical fiber and internal light delivery through its waveguide properties [15–18]. These apertureless, tip-enhanced near-field microscopy techniques do not suffer from the same sensitivity scaling law as NSOM and instead have i) high sensitivity that benefit from the optical antenna properties of the tip, ii) nanometer spatial resolution that is determined to first order by the apex radius of the tip, which can be smaller than 10 nm, and iii) a nearly unconstrained spectral range that spans from the visible to THz spectral range. In scattering scanning near-field optical microscopy (s-SNOM), far-field radiation is focused onto an AFM tip, which in turn scatters the tip-sample coupled near-field into far-field radiation that can be detected spectroscopically e.g., with tunable lasers, grating spectrometers, or Fourier transform interferometers [19–25]. An alternative technique, called photo-thermal near-field imaging (PTIR), also known as AFM-IR, detects an opto-mechanical response of the AFM tip induced by the thermal expansion of the sample with the IR-resonant absorption of pulsed or modulated incident IR light [26–28]. A related technique called photo-induced force microscopy (PiFM) was proposed to provide IR imaging contrast based on the optical gradient force between tip and sample [29]. However, the mechanism underlying the observed contrast of albeit high quality was recently suggested to also be dominated by thermal expansion rather than an optical force at least at IR wavelengths [30–32].

These new techniques have combined the chemical specificity of infrared spectroscopy with the spatial resolution and sensitivity of atomic force microscopy (AFM), extending the spatial resolution of infrared spectroscopy and imaging to the nanoscale, which is 100–1000 times smaller than the diffraction limit. The high spatial
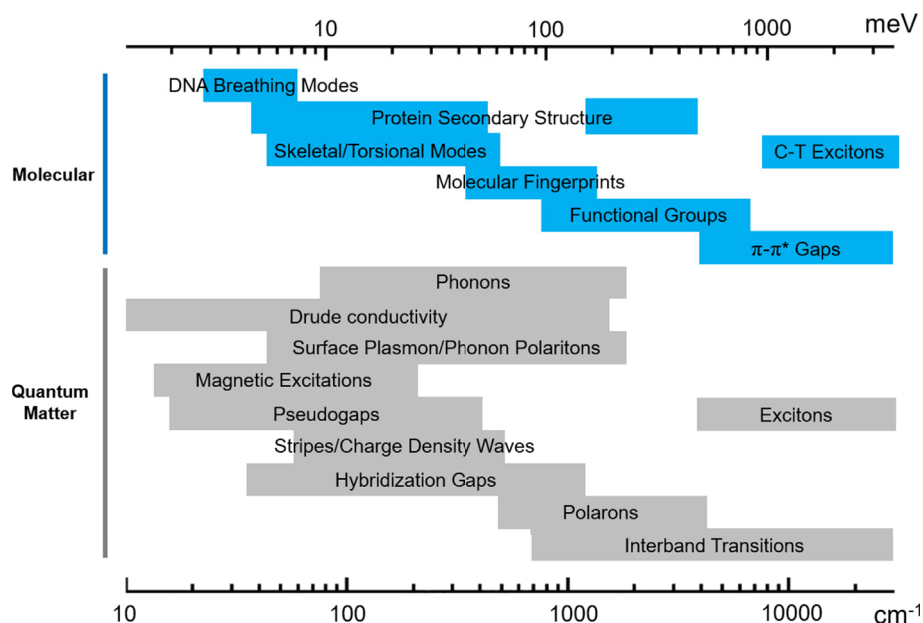
Fig. 1. Characteristic frequencies for vibrational and other low-energy absorptions throughout the infrared range. For molecular and soft materials, structural and deformation vibrational modes have energies in the far-IR/THz, "fingerprint" modes and functional group absorptions exist in the mid-IR, and π- π* and excitonic transitions occur in the near-IR/visible range. For quantum and condensed matter systems, in addition to conventional Drude free-electron behavior, the far-IR hosts a number of more exotic excitations associated with e.g. magnetic or superconducting interactions, as well as collective excitations such as bulk and surface plasmon polaritons. Lattice-related excitations such as phonon and polarons span both the far- and mid-infrared, while exciton, bandgap, and other higher-energy interband transitions span the range from near-infrared to visible. Figure adapted with permission from Ref. [2].

resolution implies a signal generated by only a nanoscopic sample volume. Thus, despite the local field enhancement provided by the tip, these techniques typically have weak signals, a large background, and an inefficient conversion of far-field irradiation into near-field excitation. As a consequence, near-field techniques are often limited by the availability of appropriate light sources, particularly in the infrared, with the need for broadband infrared nano-spectroscopy covering the mid-IR range, typically 500-4000 cm^{-1} or beyond.

Synchrotron infrared radiation is a unique source that provides broad spectral bandwidth, high spectral irradiance, coherence, stability, and a high-repetition rate. When combined with near-field IR techniques, synchrotron IR enables sensitive molecular or phonon vibrational specific chemical and quantum-state imaging with <25 nm spatial resolution, spanning the mid- to far-infrared spectral range. In this Review, we discuss the technical developments and scientific advances in the field of synchrotron infrared nano-spectroscopy (SINS), highlight recent exemplary applications for a wide range of science questions, and provide a perspective for the future extension of this technique and its expansion into new science areas. Although much of the development of SINS builds on the prior and ongoing progress of laser-based near-field techniques, a full review of infrared near-field methods is beyond the scope of this paper with selected aspects covered in earlier reviews [22−25,27,28,33]. We therefore limit this discussion to the basic principles of s-SNOM as it pertains to its implementation with a broadband source and we focus in particular on the unique aspects of synchrotron infrared radiation and the emerging field of ultra-broadband IR nano-spectroscopy and -imaging with SINS.

2. Synchrotron infrared radiation: broadband, bright, and spatially coherent

Relativistic electrons traversing a constant magnetic field are accelerated along a curved trajectory and emit electromagnetic radiation tangential to their trajectory (see Fig. 2A) [34]. This synchrotron radiation spans an extremely broad spectral range, extending from the far-IR to the X-ray regime (Fig. 2B). Because synchrotron radiation originates from a small diameter electron beam (smaller than 200 μm for modern storage rings) and is emitted into a narrow solid angle, the etendue of the source is sufficiently small such that synchrotron infrared light is diffraction-limited and spatially coherent [34,35]. The spatial coherence and large photon flux yield an infrared source that has a spectral irradiance 2−3 orders of magnitude greater than that of a typical incoherent, thermal infrared source, which usually has a source size in the mm-range and emits into a large solid angle. Moreover, synchrotron infrared radiation is linearly polarized in the plane of the orbit and circularly polarized above and below the storage ring plane, with the total degree of polarization approaching 3:1 for the in-plane and out-of-plane components, respectively, depending on the details of the radiation-extraction scheme [34].

Synchrotron light is pulsed with repetition rates typically in the 100's of MHz for standard operation modes, though pulse widths and repetition rates can vary considerably depending on the electron fill pattern and the design parameters of the storage ring. As an example, for multi-bunch operation, the Advanced Light Source (ALS) at the Lawrence Berkeley National Laboratory in California typically produces 60 ps pulses at a repetition rate of 500 MHz with a total beam current of 500 mA. Most synchrotrons worldwide utilize similar multi-bunch modes in which the repetition rate of the source is much higher than the response time of standard IR detectors, such that the source is often treated as quasi-continuous wave (CW).

Some synchrotrons, such as BESSY II in Germany or Synchrotron SOLEIL in France, have the ability to operate in a low momentum compaction factor (low-alpha) mode with a much shorter pulse width (<7 ps), enabling the generation of coherent synchrotron radiation (CSR) in the far-IR [36,37]. Unlike standard synchrotron operation modes, in which each electron radiates incoherently and the photon flux is proportional to the number of electrons (N),
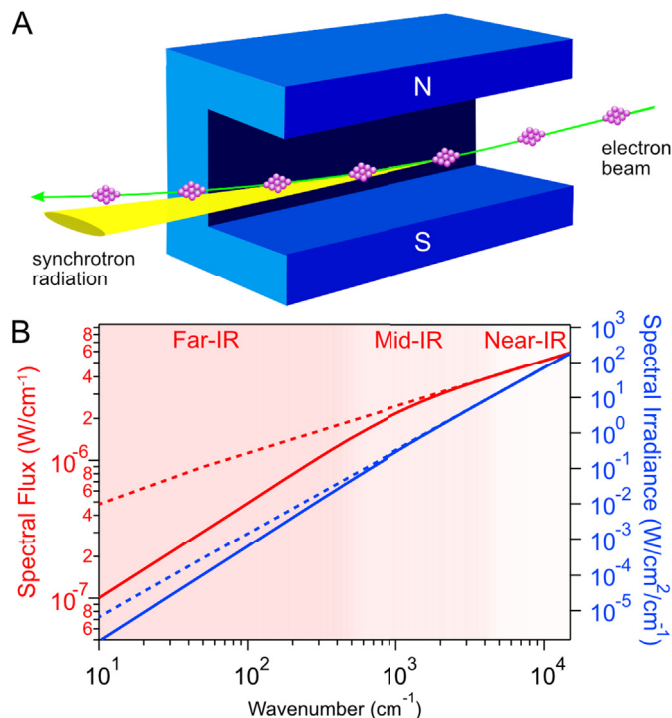
Fig. 2. Broadband light from a synchrotron source. (A) Broadband synchrotron radiation is produced when relativistic electrons are accelerated by a constant magnetic field. (B) Calculated spectral flux (red) and spectral irradiance (blue) for bend magnet radiation at the ALS, assuming a collection angle of 17 (V) mrad x 69 (H) mrad (solid line), which is standard for beamlines 2.4 and 5.4, and 80 (V) mrad x 69 (H) mrad (dotted lines), which enables the maximum extraction of the infrared light to 20 cm^{-1}. The spectral flux was calculated with the SRW package using the accelerator parameters of the ALS and the spectral irradiance was calculated assuming a diffraction limited spot size for NA = 0.4. (For interpretation of the references to color in this figure legend, the reader is referred to the Web version of this article.)

electrons in bunches shorter than the wavelength of light will radiate coherently with the photon flux proportional to N^2. Because of the 10^7-10^9 electrons in an individual storage ring bunch, CSR can generate very high power. However, the upper spectral limit of CSR is determined by how short the electron bunches can be compressed, which is typically a few ps, yielding an upper limit of ~60 cm^{-1}. The lower limit of ~1 cm^{-1} is determined by the geometrical constraints of the vacuum chamber and beamline.

The primary considerations for infrared beamline performance at modern synchrotrons are the storage ring total current and the collection angle of the beamline optics, as the spectral photon flux is proportional to both. Other considerations include storage ring stability, optical design of the beamline, and the mechanical rigidity of beamline components. Because synchrotron infrared radiation is often used in conjunction with FTIR techniques, temporal fluctuations can easily lead to spectral fluctuations at fixed frequencies. However, modern storage rings generally have fine control of the electron beam orbit and incorporate damping of floor and other mechanical vibrations to minimize these temporal fluctuations.

Synchrotrons have traditionally operated in decay mode, in which the storage ring is filled to a specified current and then allowed to decay to nominally half the original value before refilling, typically 2−3 times or more per day. In recent years, most synchrotron facilities have been upgrading to "top-off" or "top-up" operations [38], a mode where electrons are quasi-continuously injected into the storage ring to maintain a constant current. This mode of operation has obvious advantages over decay operation in terms of increased flux, constant brightness, thermal stability, and

uninterrupted light.

The natural opening angle θ_{nat} of synchrotron infrared radiation is the angle required to transmit 90% of the light at a given wavelength. For bend magnet radiation, $\theta_{nat} = 1.66188\left(\frac{\lambda}{\rho}\right)^{1/3}$, where θ_{nat} is in radians and ρ is the radius of the electron beam arc through the bend magnet in the same units as the wavelength λ[34]. The ALS bending radius, for example, is about 5 m, so for $\lambda = 10$ μm, $\theta_{nat} \cong 21$ mrad. Because θ_{nat} has a wavelength dependence, far-IR beamlines require much larger angles for efficient collection than mid-IR beamlines. Moreover, for beamlines with sufficient extraction angles, the beam size is wavelength dependent, which complicates optimal optical designs for all wavelengths. To obtain the smallest focal spot for the shortest wavelengths, the beam size should match the entrance aperture for the focusing element, whether that is a parabolic mirror or Schwarzschild objective. However, the larger beam size of the longer wavelengths will overfill the aperture and consequently have a reduced flux. Conversely, matching the beamsize of the longer wavelengths to the entrance aperture results in an underfilling of the entrance aperture by the shorter wavelengths and a sub-optimal focal spot. In practice, most infrared beamline designs choose a wavelength in the middle of the range of interest to optimize the performance of the beamline components, and compromise on the spatial resolution for the shortest wavelengths and the flux at the longest wavelengths.

3. Synchrotron IR compared to other IR sources

Heated filament or "Globar" thermal emitters are the standard source for conventional far-field FTIR spectroscopy. These approximate blackbody radiators have high bandwidth to cover the far- and mid-IR regions and are stable, inexpensive, and turn-key, which makes them practical for commercial spectrometer applications for routine use. However, thermal sources have low spectral irradiance (W/cm^2/cm^{-1}) due to their large etendue and incoherent nature. Thus, they are not ideal for high spatial resolution measurements because of the inability to focus to the diffraction-limit without the use of flux-limiting apertures. This low spectral irradiance is particularly limiting for infrared near-field experiments, where the use of these thermal sources has so far only been workable for systems that exhibit a very strong IR response [39,40]. Alternatively, plasma sources (~9000 K) operate at a much higher effective temperature than conventional thermal sources (~1400 K) and consequently have higher radiances as well as emitter areas as low as <500 μm in diameter [41,42]. Although an improvement over conventional thermal sources, the spectral irradiance and stability of these sources are still limiting for near-field applications.

Infrared laser sources have advantages over thermal sources because of their coherence properties and larger attainable spectral irradiance, albeit with limited tunability and/or spectral bandwidth. Narrowband lasers, such as quantum cascade lasers (QCL) or CO_2 lasers, offer the highest spectral irradiance needed to probe nanoscopic volumes and are well suited for imaging at a single wavelength to provide chemical contrast [24]. However, their narrow tuning range typically spans only one or a few vibrational modes and therefore limits their ability to provide chemical identification. Although quantum cascade lasers (QCL) with larger tuning ranges are becoming available, the established methods to extract near-field amplitude and phase information from a single-frequency s-SNOM experiment, such as pseudo-heterodyne [43] or two-phase homodyne detection [44], are not conducive to fast spectral acquisition. Similarly, free electron lasers (FELs) provide

intense narrowband pulses that can be tuned widely over the infrared region [45,46], providing a unique source for imaging at multiple wavelengths over a broad range. However, as is the case for all narrowband lasers, acquiring spectra by tuning the laser one wavelength at a time can be subject to systematic errors, particularly if the intensity fluctuations are large or the tune time is long.

Broadband laser sources, in conjunction with FTIR techniques, offer the possibility to increase the speed and accuracy of nano-spectroscopy experiments [24]. Broadband femtosecond-pulsed IR lasers trade both spectral irradiance and total power for increased spectral bandwidth and have recently been employed to study a variety of materials [47–55]. Pulsed laser systems based on non-linear processes, such as optical parametric oscillators (OPO), optical parametric amplifiers (OPA), or difference frequency generation (DFG), with bandwidth of ~100 cm^{-1} or more enable the investigation of a multiple vibrational modes without tuning [49,51]. Super-continuum sources have been steadily increasing in bandwidth up to the ~700 cm^{-1} range in the mid-IR, enabling the investigation of multiple resonances simultaneously, but at the cost of reduced spectral irradiance [47]. Other broadband sources have achieved bandwidths that cover a significant portion of the IR region [56,57], but the combination of spectral stability and power across the full mid-IR at high repetition rates remains difficult to achieve. Despite rapid progress in laser development towards broadband and high spectral irradiance sources, many laser systems require considerable expertise to operate and are less stable than synchrotron based light sources.

Synchrotron radiation is well-suited for infrared nano-spectroscopic measurements. The spectral irradiance and spatial coherence exceed those of a thermal source, yet the bandwidth spans the entire mid-infrared region and beyond. Furthermore, because of the nature of the source, the spectrum of synchrotron radiation is quite stable and independent of temperature, enabling repeatable full infrared spectral acquisition. However, the lower spectral irradiance, compared to many laser sources, limits its applicability with samples in which single frequency imaging or high spectral irradiance is desired or needed. Thus, in practice, a combination of single frequency and broadband sources enables the most flexibility for demanding applications.

4. Historical development of synchrotron IR near-field spectroscopy and imaging

The unique properties of synchrotron IR radiation were first recognized in the early 1970s [58]. However, to the best of our knowledge, the successful combination of synchrotron IR with an infrared microscope did not occur until the mid-1990's at the National Synchrotron Light Source (NSLS) at Brookhaven National Laboratory [59,60]. Since then infrared beamlines have proliferated worldwide, with nearly every major synchrotron having at least one infrared beamline with micro-spectroscopic capabilities. These beamlines have made diffraction-limited IR spectroscopy and imaging routine with an ultimate spatial resolution limited to λ/2, or about 2–20 μm in the mid-IR, depending on wavelength [61], and have been used to address questions in a variety of scientific areas, including materials, biological, environmental, or earth and space sciences [62–66].

The first reported coupling of synchrotron IR light to an AFM was in 2002 at the Daresbury Light Source in England, where synchrotron light was focused onto a photothermal probe on a specially designed AFM head [67]. With these exploratory measurements, improved spectral contrast on a polypropylene/poly-carbonate sample was observed with a synchrotron IR source compared to a thermal source. However, the spatial resolution of the technique with synchrotron IR was not quantified, but was

stated qualitatively that the same instrumentation had achieved a spatial resolution <5 μm with a thermal source.

In 2004, near-field THz micro-spectroscopy was demonstrated with THz coherent synchrotron radiation (CSR) from the BESSY II synchrotron source in Germany [68]. At BESSY II, up to 300 μW of stable CSR was generated in the 3-33 cm^{-1} region and then focused through conical waveguides with small exit apertures. For a 200 μm exit aperture probe, a spot size of ~130 μm was achieved, which, at a frequency of ~12 cm^{-1}, yielded a spatial resolution of λ/6. For a 100 μm aperture probe, the spatial resolution was improved to 70 μm or λ/12 at 12 cm^{-1}, albeit at the cost of bandwidth and nearly 2 orders of magnitude lower light transmission. Despite the loss in intensity, biological tissues, including leaves and teeth, could be imaged with sub-diffraction spatial resolution at these long wavelengths [69]. In 2008, aperture-based near-field measurements were extended into the mid-IR with synchrotron infrared light from SPring-8 in Japan using a cantilever probe with a 3 μm square aperture, demonstrating a spatial resolution of λ/5 at 650 cm^{-1} [70]. Although the spatial resolution of these aperture-based experiments in absolute terms was still large, these experiments demonstrated substantial progress towards sub-diffraction imaging and spectroscopy with near-field techniques using a synchrotron source. Furthermore, they demonstrated that the design of the near-field aperture probe was critical to obtaining sufficient throughput, and illustrated the difficulties of increasing spatial resolution further with an aperture-based probe.

While these initial attempts proved promising, sub-micron spatial resolution was not demonstrated until the scattering version of the near-field technique in the form of s-SNOM was adopted. In 2007, mid-IR s-SNOM at BESSY II was achieved with near-field localization of <200 nm in evanescent excitation with tip-scattered spectrally-integrated detection [71]. In 2012, synchrotron light from SPring-8 coupled to an s-SNOM attained 300 nm spatial resolution (λ/30 at ~1000 cm^{-1}) with FTIR spectra from 700 cm^{-1} to 4000 cm^{-1} on a gold/silicon test structure [72]. For these experiments, synchrotron IR light was passed through a conventional FTIR interferometer and then focused on the tip of a modified tuning-fork AFM (UNISOKU). The scattered light was collected by a parabolic mirror in an orthogonal direction to minimize background.

In 2013, synchrotron light from the Metrology Light Source (MLS) in Germany was coupled to an asymmetric Michelson interferometer integrated in a commercial s-SNOM instrument (Neaspec GmbH) [73]. With this approach, SiC/gold test structures were imaged with broadband light at <100 nm spatial resolution. Spectra of gold and the surface phonon polariton response on SiC in the 800-3500 cm^{-1} region were also reported, but the spectra above 1200 cm^{-1} showed oscillations that hindered analysis of broadband spectra. Subsequent synchrotron infrared measurements at the MLS in 2014 demonstrated an improved spatial resolution <40 nm, and spectra of SiC, SiO$_2$, TiO$_2$, and Si$_x$N$_y$ with good SNR in the range between 700 and 1200 cm^{-1} [74].

Also in 2013, broadband IR radiation from the Advanced Light Source (ALS) was used to image square loop metastructures with a spatial resolution <100 nm using a modified commercial AFM (Veeco/Bruker) [75]. After incorporating an external commercial rapid-scan FTIR interferometer (Thermo-Scientific) and the AFM into an asymmetric Michelson interferometer configuration, near-field FTIR nano-spectroscopy with a spatial resolution of <40 nm on SiO$_2$/Si test structures was demonstrated at the ALS in 2014 [76]. Furthermore, broadband amplitude and phase-resolved near-field spectra were measured on a variety of samples, including semi-conductors, bio-minerals, and protein nano-structures, covering the mid-IR region from 700 cm^{-1} to 5000 cm^{-1}. These results indicated that SINS could be used for routine user operation on a

variety of samples.

In addition to the *s*-SNOM approach, researchers have explored using synchrotron IR radiation as a broadband source for PTIR. Typically performed with tunable pulsed lasers, PTIR measures the deflection of the AFM tip upon thermal expansion of the sample, providing nanometer spatial resolution and sensitivity. The first demonstration of synchrotron IR for PTIR nano-spectroscopy was achieved in 2016 at Diamond Light Source in England using an in-vacuum mechanical chopper (50−150 kHz) to modulate the synchrotron radiation at the contact resonance frequency of the AFM cantilever. [77] This approach increased the detection sensitivity and enabled the measurement of PTIR spectra of polystyrene and cyanoacrylate films with a spatial resolution better than 500 nm at a frequency of 1650 cm^{-1}.

Since these initial instrument developments and proof of concept demonstrations of infrared nano-spectroscopy, other synchrotrons have implemented similar approaches. *s*-SNOM spectra of SiC, SiO$_2$, and Au have been recorded at SOLEIL [78,79], and plasmon-phonon coupling in graphene and h-BN have been examined at the Brazilian Synchrotron Light Laboratory (LNLS) [80]. Researchers at LNLS notably demonstrated an *s*-SNOM detection scheme based on a symmetric Michelson interferometer, using self-referenced interferometry to extract the amplitude and phase response of PMMA and PDMS thin films [81]. The successful implementation of the *s*-SNOM and PTIR approaches has opened a new paradigm for synchrotron infrared beamlines with a focus on user-supported nano-spectroscopic measurements that were previously impossible to measure with conventional far-field techniques. Section 6 describes several measurements that have progressed beyond proof-of-principle measurements and instead have addressed fundamental questions of a wide variety of natural and engineered materials by probing the chemical, biological, and physical properties at the nanoscale. To date, the spectroscopic applications associated with synchrotron PTIR are limited; therefore, the remainder of the review will focus on *s*-SNOM and its applications.

5. Scattering scanning near-field optical microscopy (*s*-SNOM)

Fig. 3 shows a schematic of a typical *s*-SNOM or nano-FTIR experimental configuration, which is generally applicable to any broadband source and has been implemented with both homebuilt and, more recently, commercial *s*-SNOM instrument platforms [2,73,74,76,79,82]. The core component is a customized or modified atomic force microscope (AFM), ideally sample scanning with the tip stationary with respect to the incident IR focus, and sufficiently
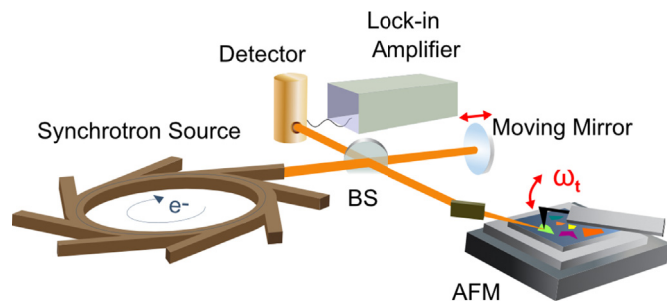

Fig. 3. SINS schematic. (A) Synchrotron infrared light enters an asymmetric Michelson interferometer, in which a beamsplitter (BS) directs half the light to an atomic force microscope (AFM) tip and the other half to a moving mirror. The backscattered light from the tip and the reference beam are recombined on the beamsplitter and detected by an IR detector and demodulated at the n-th harmonic of the tip tapping frequency ω_t.

clear open aperture to accept large numerical aperture IR optics for tip illumination. For SINS, incident synchrotron light is focused onto a typically metal-coated tip of an atomic force microscope (AFM), scanning in nanometer tip-sample force-controlled proximity to the sample, while the elastically scattered light is collected and measured with an IR detector [19,22,23]. The conductive tip effectively acts as an optical antenna by localizing and scattering the optical field in the near-field region of its nanoscopic apex. To first approximation, the spatial resolution of the technique is wavelength independent and is limited only by the tip radius, which can be <10 nm.

Because the AFM tip is smaller than the focus of light, the incident light also scatters off surfaces other than the tip apex, including the tip shaft outside the near-field tip-sample interaction region. In order to differentiate the near-field scattered signal from the larger far-field background signal, several modulation schemes have been developed [18,43,44,47,83,84]. First, the AFM is usually operated in tapping or non-contact mode where the tip-sample distance is modulated by 10's of nm's at the mechanical eigenfrequency of the cantilever ω_t, which is typically on the order of 100's of kHz. Because the near-field interaction has a highly localized nonlinear dependence on tip-sample separation, demodulating the detector signal at higher harmonics of ω_t (e.g. $2\omega_t$, $3\omega_t$, …) with a lock-in amplifier isolates the near-field interaction with increasing near-field contrast as harmonic order increases, albeit at the expense of signal strength.

Second, the AFM tip is usually incorporated into one arm of an asymmetric Michelson interferometer, such that light scattered from the tip interferes with the reflected light from a reference mirror [24]. For a broadband source, this configuration is not only desirable to spectrally resolve the source via interferometry by linearly moving the reference arm mirror by a length necessary to achieve a desired spectral resolution, but also has the added benefit of heterodyne amplification by mixing the stronger reference field with the weaker tip-scattered near-field [39,47]. The resulting IR intensity at the detector is then given by

$$I = \left(\boldsymbol{E}_{nf} + \boldsymbol{E}_{bg} + \boldsymbol{E}_{ref} \right)^2 = \boldsymbol{E}_{nf}^2 + \boldsymbol{E}_{bg}^2 + \boldsymbol{E}_{ref}^2 + 2\boldsymbol{E}_{nf}\boldsymbol{E}_{bg} + 2\boldsymbol{E}_{nf}\boldsymbol{E}_{ref} + 2\boldsymbol{E}_{bg}\boldsymbol{E}_{ref},$$

where $\boldsymbol{E}_{nf}$ is the near-field tip-mediated scattered light, $\boldsymbol{E}_{bg}$ is the far-field background scattered light, and $\boldsymbol{E}_{ref}$ is the reference field. Lock-in detection suppresses the unmodulated terms $\boldsymbol{E}_{bg}^2$, $\boldsymbol{E}_{ref}^2$, and $2\boldsymbol{E}_{bg}\boldsymbol{E}_{ref}$, yielding the tip-sample distance dependent near-field containing terms

$$I \xrightarrow{lock-in} \boldsymbol{E}_{nf}^2 + 2\boldsymbol{E}_{nf}\boldsymbol{E}_{bg} + 2\boldsymbol{E}_{nf}\boldsymbol{E}_{ref},$$

with the modulated self-homodyne signal $2\boldsymbol{E}_{nf}\boldsymbol{E}_{bg}$, the heterodyne signal $2\boldsymbol{E}_{nf}\boldsymbol{E}_{ref}$, and $\boldsymbol{E}_{nf}^2$. Because the self-homodyne signal is constant at a single tip position, it only contributes an offset to the tip demodulated signal, which is easily removed. Unlike conventional FTIR instruments that use a symmetric Michelson interferometer configuration with the sample placed after the interferometer, nano-FTIR measurements use an asymmetric configuration where the sample is placed in one arm of the interferometer. The Fourier transform of the resulting asymmetric interferogram then provides both the spectral amplitude and phase of the optical response of the sample.

To first approximation, the probing depth of the *s*-SNOM signal is determined by the spatial extent of the near-field signal from the apex, and as such is related to the tip radius. Extrinsic experimental

parameters, such as the degree of harmonic demodulation and tapping amplitude can also alter the probe depth response [85−88]. Nevertheless, as with most scanning probe techniques, s-SNOM is a surface technique with probe depths typically <100 nm and the signal is dominated by the response of the top 10−20 nm. Sample requirements are generally minimal with the primary restriction being that the samples are AFM compatible. The variety of materials that can be measured with s-SNOM is thus quite diverse. Although hard materials that interact strongly with light through collective excitations typically produce a stronger response (phonons, plasmons, etc.), even weak vibrational molecular signatures in soft, molecular, and biological materials can be measured with sufficient SNR.

5.1. Imaging modes

While the primary advantage of using synchrotron IR for s-SNOM is for nano-spectroscopic applications, the source can also be used to acquire IR images simultaneously with AFM topography. As shown in Fig. 4, there are several possible imaging modes, as illustrated with SiO_2 and Si. In the self-homodyne imaging mode (Fig. 4B), the reference arm is blocked and only the self-homodyne signal $2E_{nf}E_{bg}$ term is detected after lock-in demodulation at the desired harmonic of the tapping frequency. With a broadband source, imaging contrast is primarily nonresonant and mostly represents the changes in the dielectric permittivity ε_1 between materials, as illustrated with SiO_2 and Si. While this is the simplest imaging modality, the self-homodyne signal is typically weak for samples that are not highly reflective. More importantly, E_{bg} is of uncontrolled phase with respect to E_{ref} and can vary with sample position, causing a variation in baseline that is not necessarily chemically related to the sample. This variation is typically less evident for a broadband source than it is for a single-frequency source, but can still introduce artifacts into the image that are particularly obvious for images larger than the infrared wavelength. Additionally, local topography influences the near-field coupling strength between the tip and the sample. This local effect is background independent but still yields image and spectral amplitude intensity artifacts that are not chemically meaningful. Thus, chemical and meaningful physical effects manifest themselves only in the self-homodyne subtracted heterodyne modality and must further be analyzed beyond simple amplitude variations.

In another imaging mode, termed zero path difference (ZPD) heterodyne imaging (Fig. 4C), or "white light" imaging, the reference mirror is held at the ZPD peak of the interferogram as the sample is scanned. In this case both the self-homodyne and heterodyne signals are detected ($2E_{nf}E_{bg} + 2E_{nf}E_{ref}$). Because the self-homodyne signal ($2E_{nf}E_{bg}$) is typically much weaker than the heterodyne signal ($2E_{nf}E_{ref}$), the self-homodyne contribution to the detected signal is usually negligible. However, the self-homodyne signal can be removed by amplitude modulation of the reference beam with a chopper at frequency Ω and demodulating with the lock-in amplifier on a sideband ($n\omega_t + \Omega$), analogous to homodyne detection for a single frequency source [44]. When the reference mirror is held at the ZPD position, all frequencies are in phase and contribute proportionally to the signal according to their initial power distribution and detection efficiency. In this case, the contrast mechanism is still primarily nonresonant ε_1 dielectric contrast and from local topography. However, this approach of amplification of the near-field signal by the reference beam generally provides better contrast than self-homodyne imaging, albeit at the expense of additional experimental complexity. This method is very sensitive to mirror vibrations, thermal stability of the interferometer, and atmospheric fluctuations. The larger signal, however, enables spectrally integrated broadband imaging of many samples that could not be measured with self-homodyne imaging. Moreover, the increased SNR offers the possibility of inserting band-pass filters to select frequency bands of interest and thus provide some frequency-dependent contrast.

In a third imaging mode, called non-ZPD heterodyne imaging (Fig. 4D), a level of frequency-dependent contrast is achieved by fixing the reference mirror at a position other than the ZPD position. As in the ZPD heterodyne imaging mode, the detected signal is primarily the heterodyne signal ($2E_{nf}E_{ref}$), but with the appropriate selection of the reference mirror position, certain frequency components undergo interference, yielding frequencies that are preferentially enhanced or suppressed. This method works best with materials having phonon modes, as is the case with SiO_2, because they tend to provide stronger signals and hence provide better contrast. As shown in Fig. 4E, setting the reference mirror at the position of the red arrow, reverses the contrast between SiO_2 and Si compared to the self-homodyne and ZPD heterodyne imaging mode by preferentially enhancing the frequency associated with the SiO_2 phonon mode, which is much stronger in 25 nm thick SiO_2 than Si with a native oxide layer.

All imaging modes are performed simultaneously with AFM measurements, yielding both mechanical (topography, tapping phase, etc.) and infrared images. Scan durations depend on scan area, pixel size, and signal-to-noise requirements with scan rates typically in the 0.2−10 μm/s range and pixel dwell times in the 1−50 ms range. For all images in Fig. 4, pixel dimensions are 256 (H) × 128 (V) and were recorded with a 10 ms lock-in time constant for a total image acquisition time of ~11 min, including trace and retrace. As shown in Fig. 4F, line profiles reveal a spatial resolution of <25 nm for these images, consistent with the tip
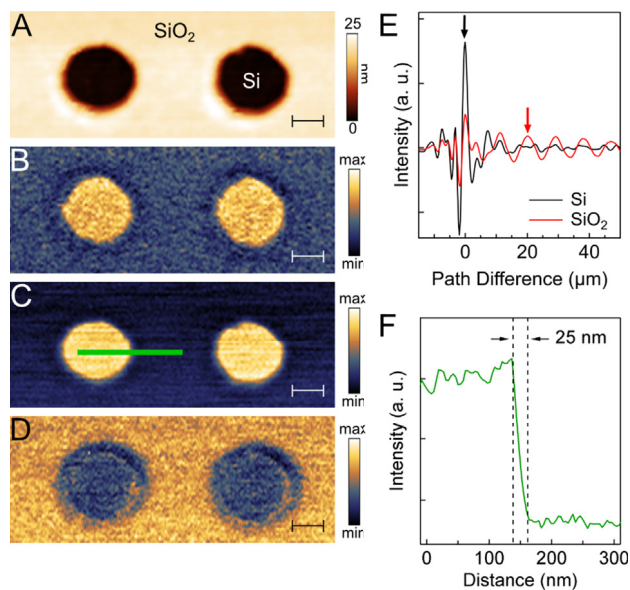

Fig. 4. Broadband IR imaging with a synchrotron source. (A) AFM topography of 21 nm thick SiO_2/Si calibration structure with Si holes. (B) 2nd harmonic self-homodyne broadband IR image acquired while blocking the reference arm in the SINS setup. (C) 2nd harmonic ZPD heterodyne broadband IR image acquired with the reference mirror fixed at the ZPD position, shown as the black arrow in (E). (D) 2nd harmonic non-ZPD heterodyne broadband IR image acquired the with the reference mirror fixed at the position shown by the red arrow in (E). The scale bar for images A-D is 100 nm. (E) Interferograms acquired on Si and SiO_2 around the ZPD position acquired while moving the reference arm. (F) Line profile across the SiO_2/Si interface of the ZPD heterodyne image, as shown by the green line in C. (For interpretation of the references to color in this figure legend, the reader is referred to the Web version of this article.)

radius of the commercial PtSi tips used for the measurements.

5.2. Broadband nano-spectroscopy

In a typical SINS experiment, AFM topography and broadband *s*-SNOM images are acquired to first locate regions of interest on the sample. Then, at selected sample locations, point spectra are acquired. To obtain sufficient SNR, multiple interferograms are typically averaged. The total acquisition time for a single spectrum with good SNR can be as short as 1 s but can be longer than 20 min, depending on the sample and measurement parameters, such as spectral resolution and harmonic detection. Although the spectral resolution for SINS measurements is technically limited only by the pathlength of the moving mirror, in practice, the spectral resolution is often limited by SNR and measurement time constraints to a few wavenumbers, typically 4-8 cm^{-1}, which is sufficient to resolve most molecular features. Likewise, although higher harmonic detection is possible, 2nd harmonic detection is typically the best compromise between far-field background suppression and SNR. Under normal SINS conditions, 2nd harmonic spectra of strong phonon modes in hard matter can be acquired at 8 cm^{-1} resolution in under 3 min, whereas 2nd harmonic spectra of molecular features in soft matter can take longer than 10 min at 8 cm^{-1} spectral resolution. For many heterogeneous materials, single spectra are insufficient to characterize the sample. One of the primary advantages of infrared micro-spectroscopy is the ability to obtain 3D hyperspectral images, where a full broadband spectrum can be acquired at each pixel of an x-y image. Automated spatio-spectral line and area nano-spectroscopy scans can be achieved by collecting spectra at each pixel, yet imaging time scales as N^2 with N-pixels in x and y directions. For this reason, one dimensional line scans are often more practical, particularly given the constraints of beamtime.

While the synchrotron source and its alignment are quite stable and reproducible for hours, and therefore enable long acquisition times, the primary challenge for acquiring long line or large area maps is sample drift. Thermal fluctuations of the sample and its mount can be as large as 30 nm per minute when the sample is first placed on the AFM stage. Sample drift is typically reduced to ~1 nm per minute after some equilibrium time (1−2 h), yet can still degrade the spatial resolution and distort an image for long acquisition times. To reduce the time of the image acquisition, line or area scans can be performed at lower spectral and/or spatial resolution and with reduced SNR.

5.3. Spectral range

Synchrotron radiation from a bend magnet is spectrally broad, spanning the far-IR to X-rays. However, the useable spectral range for *s*-SNOM with a synchrotron source is determined by the choice of beamsplitter and detector. Fig. 5 shows the *s*-SNOM amplitude spectrum on a gold reference sample for two different beamsplitter/detector configurations. Because gold has a spectrally flat response in the IR, the spectrum reflects the instrumental response, including source distribution, detector response, beamsplitter, tip coupling, the absorption of a diamond window in the beam path, and atmospheric absorption (e.g., water vapor and carbon dioxide). For mid-IR applications, KBr/Ge or ZnSe beamsplitters are often used with spectral coverage into the near-IR with low-frequency cutoffs of ~400 cm^{-1} and ~500 cm^{-1}, respectively. Thallium bromide (KRS-5) and Si beamsplitters extend the spectral coverage into the far-IR with low-frequency cutoffs of ~200 cm^{-1} and ~10 cm^{-1}, respectively.

Suitable detectors for SINS applications require high sensitivity (<10 pW/$\sqrt{Hz}$), fast response (≥1 MHz), and a spectral range
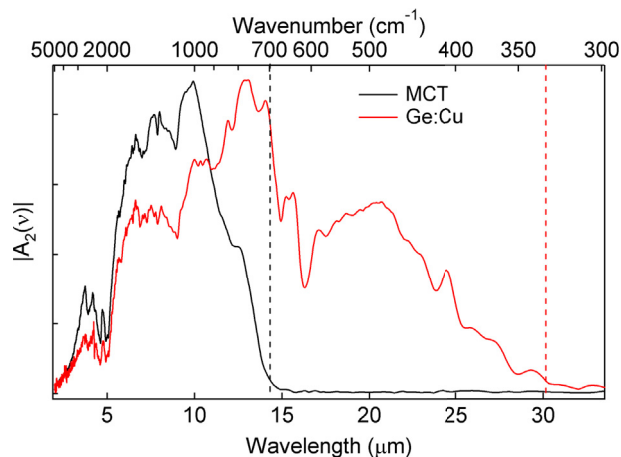

Fig. 5. Spectral range. 2nd harmonic amplitude spectra on gold with different beamsplitter-detector combinations: KBr/Ge beamsplitter with MCT photodiode detector (black) and Si beamsplitter with Ge:Cu detector (red). The spectra have been scaled such that the maximum values are equivalent. Figure adapted with permission from Refs. [2]. (For interpretation of the references to color in this figure legend, the reader is referred to the Web version of this article.)

suitable for the region of interest. Mercury cadmium telluride (MCT) photodiode detectors with elements ≤ 100 μm in size and with low frequency cutoffs near 700 cm^{-1} offer the highest sensitivity for broadband mid-IR measurements. Detection at frequencies down to ~400 cm^{-1} can be achieved by varying the concentration of the three components, Hg, Cd, and Te, in MCT photoconductor detectors, albeit at the expense of detector sensitivity by an order of magnitude or more. Extension to lower frequencies in the far-IR, however, remains challenging. Conventional far-IR detectors, such as silicon bolometers, are highly sensitive (<0.1 pW/$\sqrt{Hz}$) in this range, but typically have a maximum detector response (~1 kHz) that is too slow to respond to the AFM tip modulation. Impurity doped germanium photoconductive detectors have proven to be suitable for *s*-SNOM applications in the far-IR. Notably, Ge:Cu has been used with a broadband response down to ~330 cm^{-1} and a detection response >1 MHz [2]. Ge:Ga detectors have also been used with FEL sources to cover a more limited spectral range of 100−300 cm^{-1} and slower response rate (~200 kHz) [45,46].

Although the broad spectral range of the synchrotron source is advantageous for nano-spectroscopic measurements, the extra bandwidth beyond the region of interest can contribute to baseline noise. When operated in the asymmetric Michelson configuration, the relatively high power of the reference arm can easily saturate the detector. By spectrally filtering the input about the region of interest, the reference arm power can be reduced, resulting in increased signal to noise ratios [89]. Alternatively, reference arm attenuation can be achieved through the use of apertures and mesh filters.

5.4. Signal interpretation and modeling

As is the case for dispersive FTIR [90,91] and IR spectroscopic ellipsometry [92], *s*-SNOM performed in an asymmetric Michelson interferometer offers a means to extract the complete dielectric response of the sample. The complex valued Fourier transformed near-field spectra, typically recorded as $|A|(\bar{v})$ and $\Phi(\bar{v})$, or $Re(\bar{v})$ and $Im(\bar{v})$, can be used to determine the complex dielectric function $\tilde{\varepsilon} = \varepsilon_1 + \varepsilon_2$ or the complex index of refraction $\tilde{n} = n + ik$. The near-field measurement of $\tilde{\varepsilon}$ or $\tilde{n}$ directly relates to chemical identity and local chemical environment through the resonant response, including

localized molecular vibrations, extended phonons, other low-energy lattice or electronic excitations, and, e.g., Drude free-carrier response.

The near-field signal response is determined by the source, detector, beamsplitter, and tip interactions. To remove the contributions of the source, detector, and beamsplitter, near-field spectra are normalized to a reference material that has a spectrally flat response in the bandwidth of interest. Gold is the most common reference material because it is both spectrally flat and has strong scattering signals across the entire infrared region. Other highly reflective materials, including metals, have also been used as reference materials. Silicon is another common reference material, but the native silicon dioxide layer can contribute to artifacts in the region around 1200 cm^{-1}. The complex sample spectrum is divided by the complex reference spectrum such that the amplitudes are divided and the phases are subtracted.

When analysis is limited to nanoscale chemical identification, it is often sufficient to include only a single component IR s-SNOM signal. The s-SNOM $Im(\bar{v})$ and $\Phi(\bar{v})$ spectra are very similar and have been used as approximate measures of the material extinction coefficient $k(\bar{v})$, which can be used to identify specific marker resonances of characteristic molecular vibrations [24]. For a more quantitative measurement of the sample optical response, however, this approximation becomes insufficient. As is also the case in ellipsometry, FTIR microscopy, and grazing incidence FTIR, accurate line shapes can only be recovered in s-SNOM by measurement of the full complex-valued spectra. s-SNOM further requires accounting for the details of optical illumination, the near-field interaction between tip and sample, and the sample thickness [93].

Many analytical models have been proposed and utilized to calculate the effect of tip-sample coupling on the measured s-SNOM spectra to quantitatively extract the complete dielectric response of the sample. Significant effort has gone into understanding the effect of tip shape and material on the measured line shapes, with models ranging from the simple point-dipole model for a sphere-shaped metal tip above the sample surface [94,95] to more complex elongated spheroid models [96–98]. While the more complex models have better agreement with experiment than the point-dipole model for both molecular vibrational modes and surface phonon modes, the more complex models also include additional fitting parameters and ad hoc assumptions about the sample.

Analytical models incorporating the tip shape also usually assume that the sample is a single layer and has infinite lateral size to reduce the complexity of the system. Therefore, samples with nanoscale inhomogeneities or multi-layer systems require more complex models that are more difficult to analyze and interpret [99–102]. Numerical models have been developed to address sample inhomogeneity and include realistic tip geometries, tip-sample interactions, and signal processing procedures [103]. However, for many nanomaterials in which electron or phonon confinement and sample geometry control the physical behavior of the material, details of the sample geometry outweigh any effect of tip shape. In such nanomaterials the most important factors in modeling relate to an accurate description of physical phenomena within the sample, which we discuss below for selected cases [80,104–107].

5.5. Harmonic detection and tapping amplitude

The tapping amplitude and degree of harmonic detection can also have a measurable effect on the s-SNOM spectra [87,88]. In general, higher harmonics better discriminate the near-field signal from the far-field background and provide more surface sensitivity

at the expense of SNR. Fig. 6A compares SINS spectra of 108 nm thick SiO_2 on Si, normalized to Si spectra collected at different harmonics of the tip tapping frequency. With higher harmonic detection, the phonon mode appears to narrow and strengthen with respect to the response of silicon. The tip-tapping amplitude affects SiO_2 spectra in a similar way, as shown in Fig. 6B, with decreased tapping amplitude spectra becoming more narrow compared to the response of silicon. In general, increasing the tapping amplitude increases the demodulated signal strength, but also decreases localization, thereby reducing surface sensitivity. Further, increasing the tapping amplitude too much can cause anharmonic mechanical motion of the tip cantilever and introduce far-field artifacts into signals detected at higher harmonics of the tip-tapping frequency. Higher tapping amplitudes are also associated with tip damage and further artifacts resulting from blunt and malformed tip apex shapes. On the other hand, very small tip-tapping amplitudes reduce SNR ratios and lead to unstable AFM scanning.

In practice, for most samples, 2nd harmonic detection is a good compromise between background suppression and SNR. Similarly, we find that peak-to-peak tip-tapping amplitudes of 40−100 nm provide a sufficient compromise, enabling good SNR, reasonable surface sensitivity, stable AFM scanning, and sufficient far-field background suppression.

5.6. Tip contamination

Commercial AFM tips are often delivered with organic and inorganic contaminants, originating both from the manufacturing process and from the gel packs in which the tips are often shipped [108]. The primary contaminant is polydimethylsiloxane (PDMS) and other silicone oil variants. Signatures of PDMS are routinely seen in SINS spectra, particularly when measuring reference
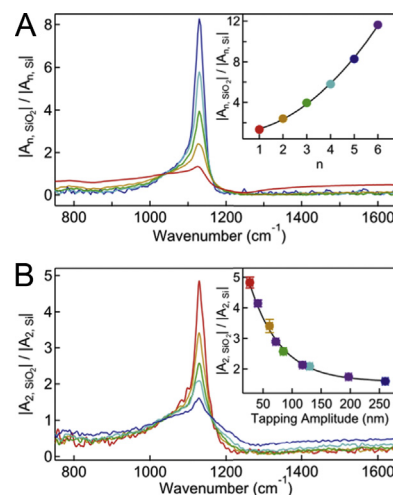

Fig. 6. Effect of harmonic detection and tapping amplitude on SiO_2 phonon mode. (A) SINS amplitude measurements of 108 nm thick SiO_2 on silicon detected at different harmonics (n) of the tip tapping frequency with a constant peak-to-peak tapping amplitude of 75 nm, normalized to the response on silicon. (Inset) Amplitude ratio of SiO_2 to Si at $\bar{v} = 1130$ cm^{-1} as a function of harmonic lock-in frequency. The individual points are color-coded to match the spectra, with the purple data point (6th harmonic) not displayed as a spectrum. The black curve is a quadratic fit to the points and serves as a guide to the eye. (B) SINS amplitude measurements of a 108 nm thick SiO_2 on silicon detected at different tip tapping amplitudes with n = 2, normalized to the response on silicon. (Inset) Amplitude ratio of SiO_2 to Si at $\bar{v} = 1130$ cm^{-1} as a function of tip tapping amplitude. The individual points are color-coded to match the spectra, with the purple data points not displayed as spectra. The black curve is an exponential decay fit and serves as a guide to the eye. (For interpretation of the references to color in this figure legend, the reader is referred to the Web version of this article.)

spectra on bare gold. As shown in Fig. 7, the SINS phase spectra agree well with ATR spectra of the gel pack and with FTIR library standards of PDMS. Approach curves, in which the sample is slowly raised toward the tip, indicate that these PDMS spectral signatures occur only within 15 nm of the tip-sample interface and exhibit a strong near-field enhancement. Because these features are strongest on gold, which is often used as a reference, and weaker on almost every other sample, they can create negative peak artifacts in normalized spectra. Various methods have been explored to remove the contamination, including ultraviolet ozone and piranha acid treatments. Although both methods effectively remove the PDMS signatures, they can introduce other contaminants and reduce the tip stability due to changes in the hydrophilicity of the tip. We note that when tips are replaced in gel packs after cleaning, noticeable PDMS contamination appears within an hour and increases over a 24-h period.

6. Applications

Infrared spectroscopy can identify and analyze a wide range of excitations and resonances of materials. Materials range from molecular, polymeric, and biological materials to inorganic semiconductors, metals, and correlated matter. Likewise, SINS is equally applicable to the same kinds of materials and, despite being a new technique, has already been utilized across various scientific fields, including biology, chemistry, plasmonics, electrochemistry, and material science. In the following, we highlight several recent SINS applications that are representative for different classes of materials that show either the first demonstration of a particular application development or especially outstanding performance. The selection is necessarily incomplete.

6.1. Chemical nano-spectroscopy of biological and natural materials

SINS has proven especially powerful as a non-destructive, nanospectroscopic probe in natural mineralogical and geochemical systems for the study of organic-mineral interfaces and interactions on the nanometer scale. As examples, these systems include the growth, life cycle, and biomineralization process of marine species and the migration and distribution of petroleum hydrocarbons in nanoporous low-permeability host rock networks. In one of the first SINS applications, the heterogeneity of calcite and aragonite in a mussel shell (blue mussel, *M. edulis*) was explored through the IR spectroscopic characteristics of the calcium carbonate ($CaCO_3$) polymorphs [76]. In this system, the formation of calcite or aragonite reflects a number of environmental parameters [109]. While the AFM topography (Fig. 8A) of a polished shell cross-section only qualitatively illustrates the different morphological structures of the two polymorphs, SINS spectra (Fig. 8B) unambiguously identify and readily distinguish the two $CaCO_3$ polymorphs through the differences in the characteristic resonance frequencies of the $CaCO_3$ out-of-plane bending ν_2 and the doubly degenerate asymmetric stretching ν_3 modes of calcite and aragonite [110]. The broad bandwidth of the synchrotron source enables the resolution of both modes simultaneously and further enables the assessment of any sample contamination, organic inclusions, or other mineral phases
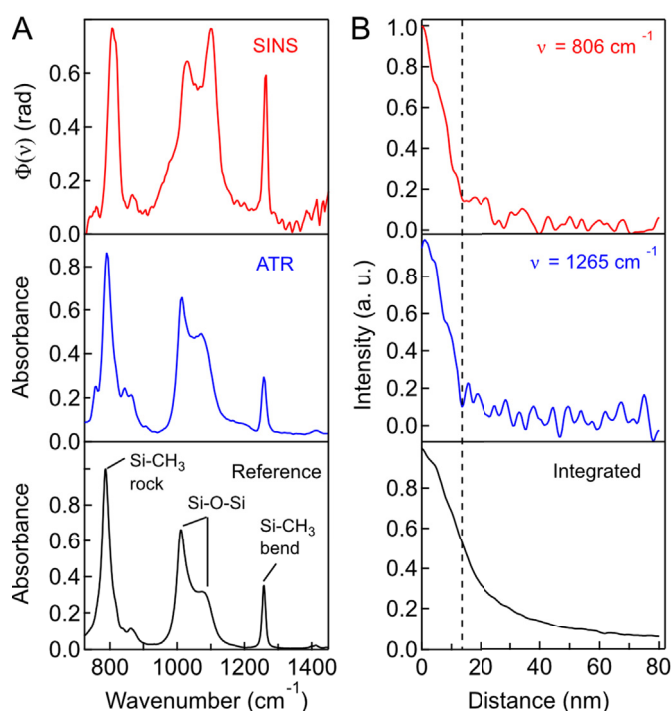

Fig. 7. Contamination of commercial AFM tips. (A) 2nd Harmonic SINS phase spectra acquired on clean gold substrate (red, top panel); attenuated total reflectance (ATR) FTIR spectra of gel-pack that AFM tips were shipped in (blue, middle panel); and library FTIR reference spectrum of polydimethylsiloxane (PDMS) (black, bottom panel). (B) 2nd harmonic SINS spectrally-resolved amplitude approach curves on template-stripped gold substrate: Si-CH$_3$ bend at ~806 cm^{-1} (red, top panel); Si-CH$_3$ rock at ~1265 cm^{-1} (blue, middle panel); and integrated region 700-5000 cm^{-1} (black, bottom panel). The vertical dashed black line at x = 14 nm indicates the point where the contamination signal grows above the noise level. (For interpretation of the references to color in this figure legend, the reader is referred to the Web version of this article.)
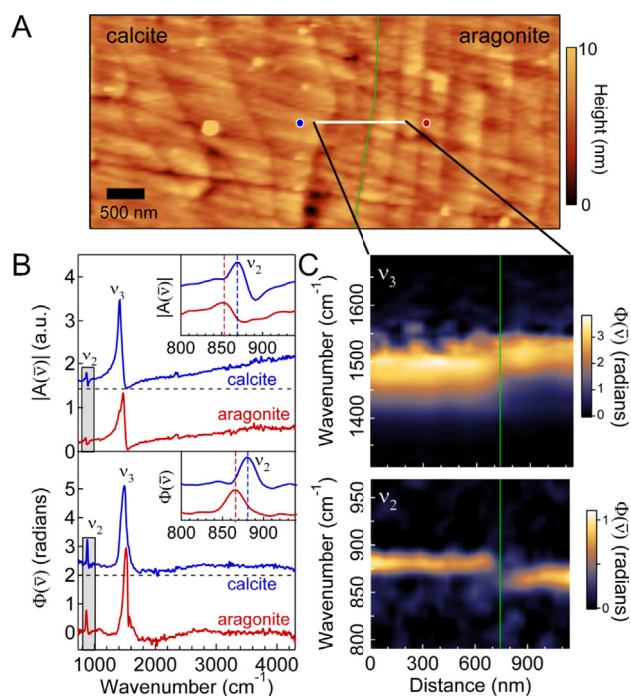

Fig. 8. $CaCO_3$ polymorph heterogeneity in a polished *M. edulis* shell. (A) AFM topography in the interface region of calcite (left), appearing with a globular morphology, and aragonite (right), appearing as stacked tablets. The green line indicates the interface between calcite and aragonite. (B) SINS $|A(\bar{\nu})|$ and $\Phi(\bar{\nu})$ spectra of calcite (blue, offset for clarity) and aragonite (red) at 8 cm^{-1} spectral resolution acquired at the location of the blue and red circles, respectively, in A. (Insets) Zoom-in of ν_2 mode (gray box) for calcite (blue) and aragonite (red) with the dashed lines indicating the peak positions. (C) Spatio-spectral SINS linescan $\Phi(\bar{\nu})$ plot across the solid white line in A. Each of the 30 spectra was acquired for 3 min at 8 cm^{-1} spectral resolution. Figure adapted with permission from Ref. [76]. (For interpretation of the references to color in this figure legend, the reader is referred to the Web version of this article.)
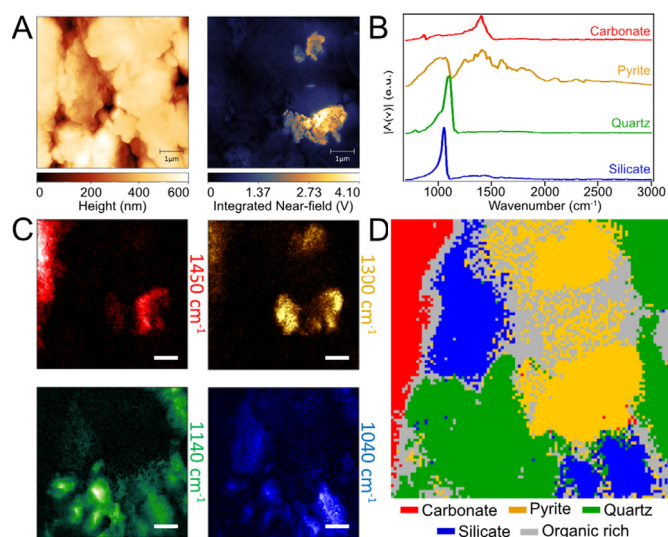
Fig. 9. Mineralogy in shale. (A) Topography map of the same area as in the hyperspectral maps. The scale bars are 1 μm. (B) Representative spectra for minerals in sample. (C) Nanometer hyperspectral maps with SINS. The maps are reconstructed from the absorbance peak areas at 1450 cm^{-1} for carbonate, around 1300 cm^{-1} for pyrite, 1140 cm^{-1} for quartz, and 1040 cm^{-1} for silicates. Scale bar 1 μm. (D) Multivariate correlative classification mapping from images in C. Figure adapted with permission from Ref. [111].

through their characteristic spectral features. Fig. 8C shows a corresponding spatio-spectral linescan of the interface region along the solid, white line in Fig. 8A, highlighting the sharp transition (<100 nm) between calcite and aragonite.

SINS has also been used to spatially resolve the organic and mineral heterogeneity of shale at the nanometer and micrometer length scales [111]. A hyperspectral image covering a 6×6 μm^2 area was obtained from the acquisition of rapid low spectral resolution

(32 cm^{-1}) spectra. Fig. 9B shows individual SINS spectra at locations with distinct spectral features that were assigned to quartz, carbonate, clay, and iron sulfide components. Single frequency images extracted from the hyperspectral image, as shown in Fig. 9C, then identify the sample texture and heterogeneity of its chemical makeup. The true advantage of collecting hyperspectral data, however, is the ability to perform multivariate analysis on the sample, using all frequencies to unambiguously identify chemical components and detail their distribution at the nanoscale.

By probing infrared-active molecular vibrations, SINS provides chemically specific molecular identification similar to conventional IR micro-spectroscopy but with nanometer spatial resolution. Localized near-field enhancement and antenna coupling enable sub-zeptomolar sensitivity for the nanoscopic probe volumes, pushing the sensitivity toward the single protein or molecular aggregate level [76]. For proteins, the vibrational signatures of amide I (center frequency: 1620-1700 cm^{-1}), amide II (1500-1560 cm^{-1}), and amide III (1200-1350 cm^{-1}) provide chemical identification and structural information [112]. As an example, Fig. 10A shows SINS spectra of dried bovine serum albumin (BSA) and γ-globulin proteins deposited on a silicon substrate, demonstrating small but clear differences in the amide I and amide II modes (1650 cm^{-1} and 1530 cm^{-1} respectively) between the two constituents. These differences are consistent with far-field IR spectra and are a signature of the protein's secondary structure. The secondary structure of BSA is primarily α-helices, whereas the secondary structure of γ-globulin is predominantly β-sheets. SINS is thus capable of measuring protein folding with nanoscale spatial resolution, which enables investigations of protein aggregation, e.g., in neurodegenerative diseases, such as Alzheimer's, Parkinson's, and Huntington's diseases.

Such SINS measurements of the different amide bands, as well as other IR vibrational markers in the fingerprint range, have been used to provide detailed molecular level insight into biological samples [113–116]. Fig. 10B and C shows the distribution of local
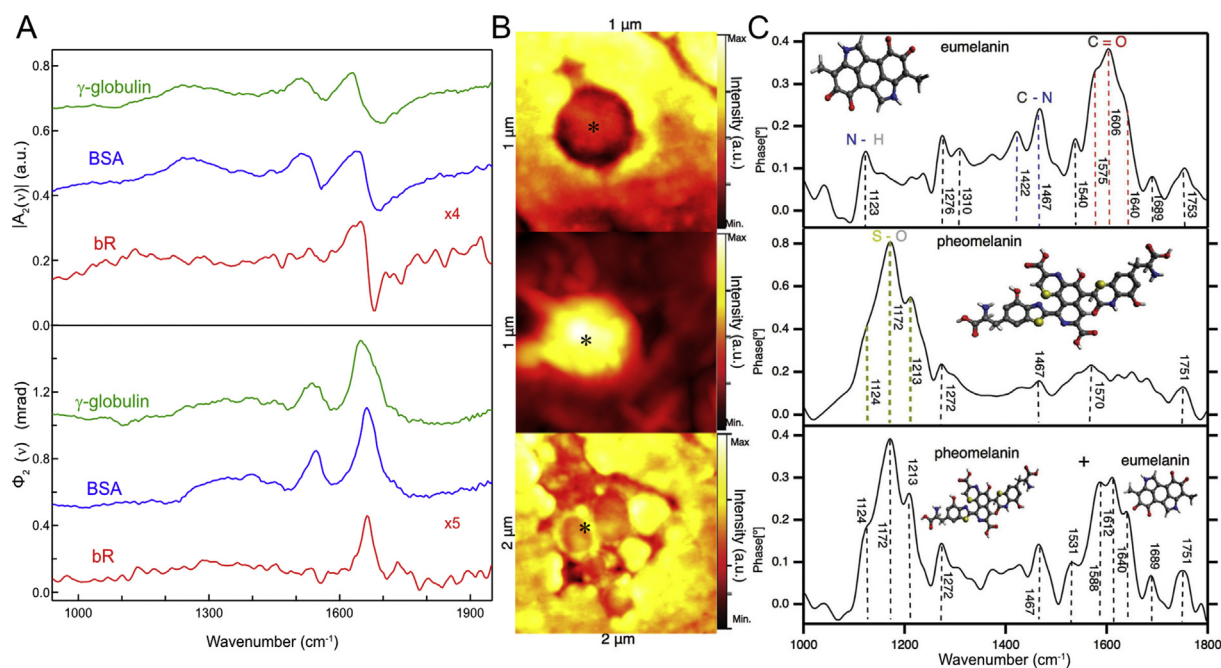

Fig. 10. Vibrational spectra of proteins and *in situ* measurements of melanosomes in hair. (A) SINS $|A(\bar{v})|$ and $\Phi(\bar{v})$ spectra of γ-globulin (green), bovine serum albumin (BSA, blue), and bacteriorhodopsin (bR, red). (B) In situ SINS images of melanosomes in the cortex of sheep hair, with markers indicating the location of acquired spectra. (C) SINS $\Phi(\bar{v})$ spectra of eumelanin (top panel), pheomelanin (middle panel) and a mixture of eumelanin and pheomelanin (bottom panel). Figure adapted with permission from Refs. [113]. (For interpretation of the references to color in this figure legend, the reader is referred to the Web version of this article.)

cellular structures through broadband SINS nano-imaging of black and white sheep hair [113]. The chemical specificity of SINS distinguishes and characterizes the melanosomes, pheomelanin, and eumelanin, while isolating and probing their native vibrational states in individual structures. By comparing black sheep hair to white sheep hair, which does not contain melanosomes, the distinct response of the native keratin filaments could be isolated.

In another example, laser-based *s*-SNOM and SINS have been used in conjunction to investigate single collagen fibrils, which are a major component of skin, bone, tendon, and cartilage in many life forms [116]. By examining collagen at the single fibril level before and after damaging mechanical stress, structural changes reveal the remarkable toughness of connective tissues and the inflammatory and healing responses to injury.

6.2. Molecular order, orientation, and IR nano-crystallography

The order and orientation of molecules are often critical structural parameters that affect the function of biomaterials (e.g. collagen), engineered molecular materials, and quantum materials. The metallized AFM tip in SINS localizes and enhances the optical field preferentially parallel with respect to the tip axis, resulting in an anisotropic optical tip scattered response that is sensitive to molecular orientation. Specifically, the tip enhances signals from vibrations that have dipole moments aligned perpendicular to the sample surface (parallel to the tip) with only small signal contribution from vibrations that have dipole moments aligned parallel to the sample surface (perpendicular to the tip) [50,104]. This

sensitivity to vibrational dipole moment orientation is demonstrated in Fig. 10A, in which the SINS spectrum of the dried purple membrane protein bacteriorhodopsin (bR) shows a pronounced amide I peak, while the amide II peak is negligible. In this case, the amide I transition dipole (C=O stretch) has a large component along the substrate normal, whereas the amide II mode (N-H stretch) is oriented parallel to the surface, thus revealing the ordered arrangement of bR in the lipid bilayer [44,50]. In contrast, the sample preparation of the γ-globulin and bovine serum albumin proteins in Fig. 10A results in randomly oriented proteins such that the SINS spectra show both amide vibrations.

For unknown samples that are highly ordered, the lack of certain vibrational features associated with the anisotropic tip response in SINS could complicate molecular identification. However, this feature can also be exploited to measure the molecular bond orientation with nanometer spatial resolution [104]. As shown in Fig. 11, in the organic electronic material perylenetetracarboxylic dianhydride (PTCDA), the C=O functional groups have dipole moments in the plane of the molecule, whereas the C-H bending modes have dipole moments that are out of the plane of the molecule. The measurement of the relative strength of these vibrational modes provides a mechanism to determine the orientation of the perylenetetracarboxylic dianhydride molecule in thin films relative to the substrate. Thus, SINS measurements can reveal structural and orientational heterogeneities that control the molecular electronic properties in devices of these organic semiconductor materials, which are difficult to image with many other techniques. This analysis has been extended to other molecules and
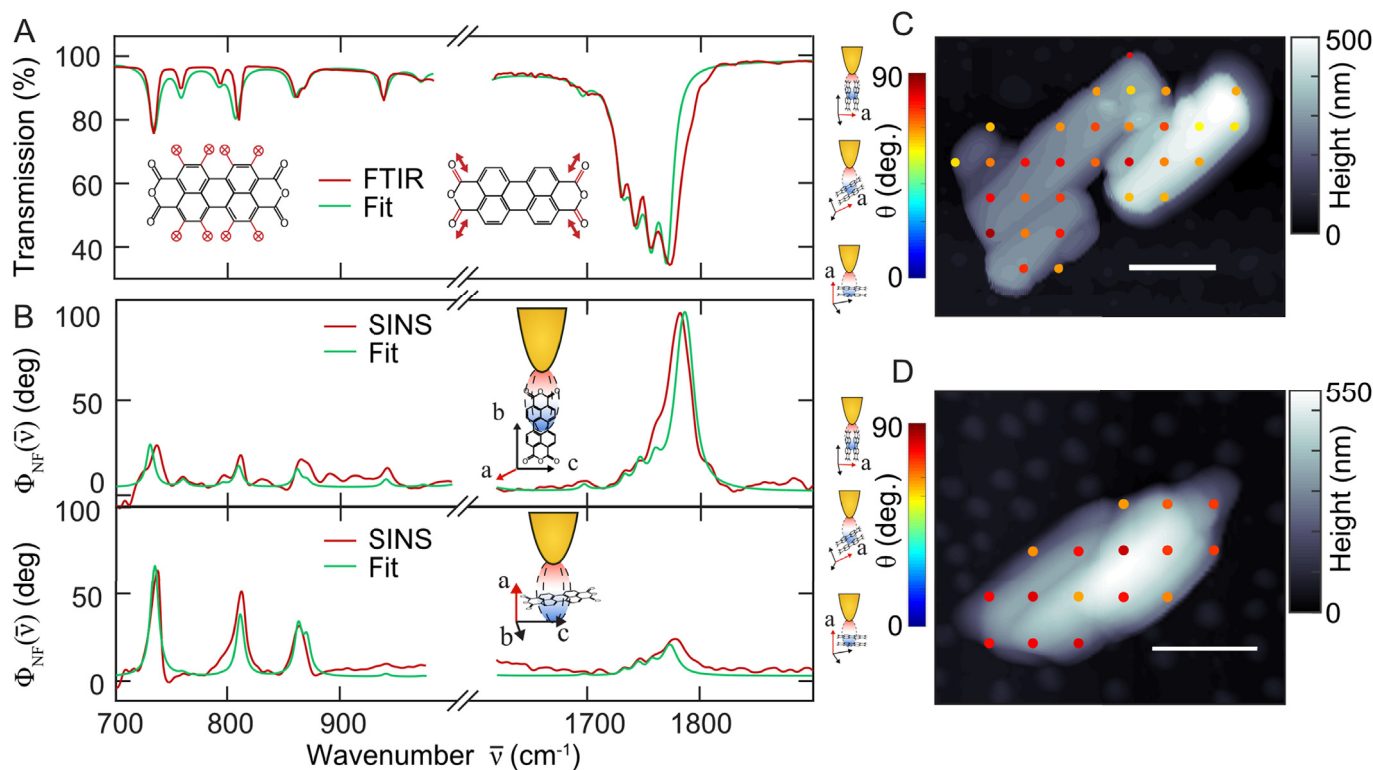

Fig. 11. Broadband IR *s*-SNOM of large crystallites. (A) Far-field transmission spectrum of dispersed PTCDA particles, fit to calculated reflectance using the Lorentz model. Inset: Schematic of C−H out-of-plane vibrations and C=O stretch of the anhydride. (B) SINS spectra (red) collected at two different nanoscale locations with (green) fit to spherical dipole model with Lorentz oscillators. (C and D) Molecular orientation is measured from SINS spectra in a spatial map across large crystals of PTCDA. Point spectra (circles) show fits of point spectra for θ, represented on a false color scale. Scale bars, 500 nm. Figure adapted with permission from Ref. [104]. (For interpretation of the references to color in this figure legend, the reader is referred to the Web version of this article.)

can provide insight into structure-function relationships, including defect formation and propagation [104,113].

6.3. Single particle measurements

The nanometer localization and high sensitivity of SINS enables measurements of single particles that were previously difficult, if not impossible, to measure with far-field IR techniques because of the lack of contrast within the far-field diffraction limited probe volume. Moreover, the improved spatial resolution of SINS enables measurement of heterogeneity within a population that cannot be revealed through bulk analysis. As an example, doped metal oxide nanocrystals were measured with traditional far-field IR techniques and SINS [117,118]. SINS measurements of aluminum-doped zinc oxide revealed linewidths as narrow as 600 cm^{-1}, suggesting that the much larger ensemble linewidths from traditional far-field FTIR measurements were heterogeneously broadened. This work shows the applicability of SINS to probe a wide range of nano-structures supporting localized surface plasmons (SPP), taking advantage of the high spectral bandwidth of synchrotron infrared radiation to measure the tunable and relatively broad spectral SPP response.

As another example, chemical reactions on single particle gold and platinum catalysts were measured with the high spatial resolution of SINS to reveal site specific enhancement of reactivity (Fig. 12) [119]. In these measurements, N-heterocyclic carbene molecules were anchored to catalytic particles and the chemical distribution of the particles was spectroscopically measured with SINS after exposure to oxidation or reduction conditions. The broad bandwidth of SINS enabled the simultaneous measurement of reactants and products and showed the transformation of NO$_2$ functionalized carbene molecules to NH$_2$ functionalized carbene molecules as well as increased reactivity at the edges of the particle. This work demonstrates the potential of SINS to probe kinetic processes and catalytic reactions of systems responding to changing environmental or chemical conditions.
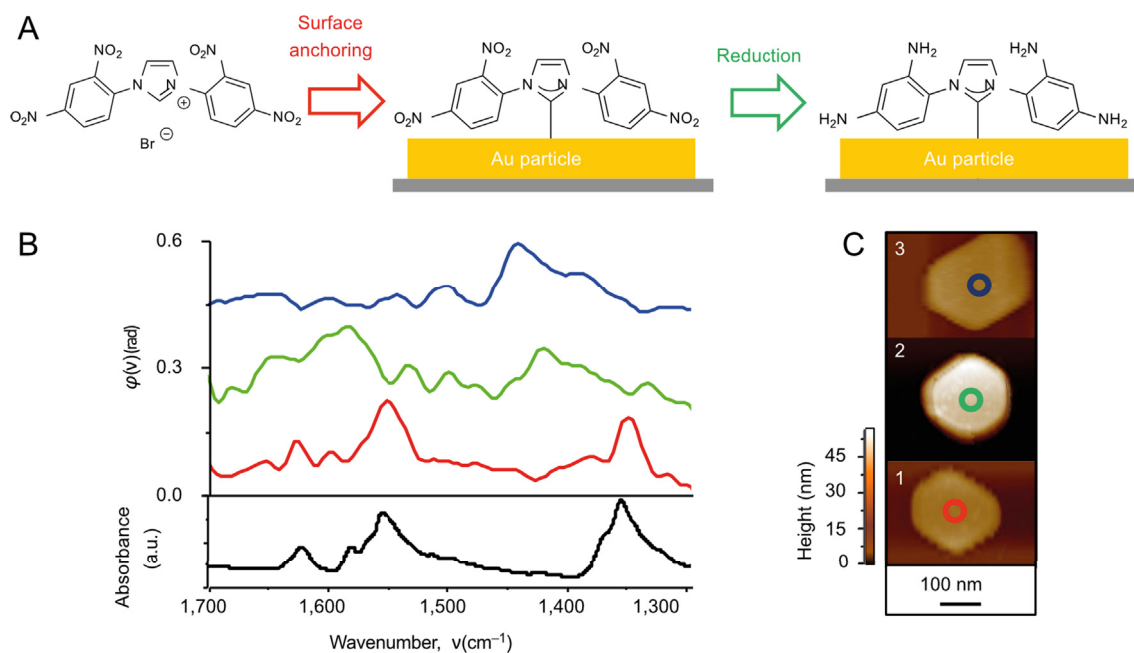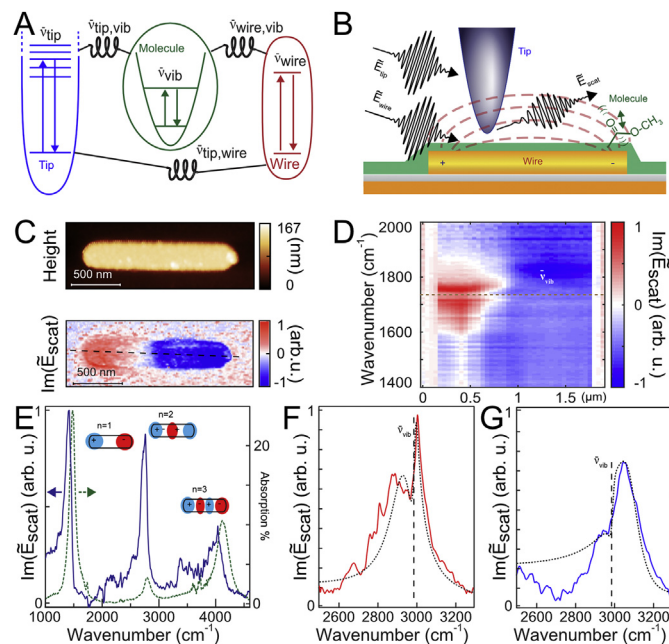

Fig. 13. Molecular vibration and antenna coupling. (A) Nanotip, nanowire, and molecular vibration are coupled in the near-field with coupling strengths $\bar{v}_{tip,wire}$, $\bar{v}_{wire,vib}$, and $\bar{v}_{tip,vib}$. (B) Conceptual experimental implementation with nanotip positioned above the nanowire with PMMA molecular thin film. (C) AFM topography (top) and s-SNOM (bottom) image of Im($\bar{E}_{scat}$) at 1775 cm^{-1} as a function of nanotip position above the nanowire. Scale bars 500 nm. (D) Spectrally resolved transect of Im($\bar{E}_{scat}$) along dashed line in C. (E) Fundamental and overtone resonances (n = 1,2,3) of the nanowire (dashed green) measured by FTIR. Im($\bar{E}_{scat}$) (solid blue) with nanotip positioned above the nanowire terminal. (F) Im($\bar{E}_{scat}$) for n = 2 response with $\bar{v}_{wire}$~2790 cm^{-1} with corresponding calculated fit (dotted). (G) Im($\bar{E}_{scat}$) for $\bar{v}_{wire}$~2960 cm^{-1} with corresponding calculated fit (dotted) to EIS. Figure adapted with permission from Refs. [106]. (For interpretation of the references to color in this figure legend, the reader is referred to the Web version of this article.)

Fig. 12. Catalytic reactions on a nanoparticle. (A) Schematic representation of the experiment. (B) Solution-phase ATR-IR spectrum of inactivated NO$_2$-functionalized imidazolium salt (black spectrum). SINS phase spectra on single Au particles: red, adsorption of NO$_2$-functionalized NHCs; green, exposure of the sample to a reducing agent (NaBH$_3$CN); blue, exposure of the sample to a deuterated reducing agent (NaBD$_3$CN). (C) AFM topography images showing the locations on the Au particles of the SINS point measurements (colored circles). The colors of the circles correspond to the colors of the spectra in B. Figure adapted with permission from Ref. [119]. (For interpretation of the references to color in this figure legend, the reader is referred to the Web version of this article.)

6.4. Metamaterials and antennas for molecular coupling

Optical metamaterials are engineered structures that achieve electromagnetic properties not native to the material that are tunable through changes in size, shape, and confinement of its mesoscopic building blocks. The ability of metamaterials in the form of optical antennas and resonators to enhance light-matter interactions has been explored with synchrotron based micro-FTIR spectroscopy to measure the full broadband response of individual antennas in the far-field, often covering the fundamental dipole resonance as well as higher order modes [75,120]. Surface-enhanced infrared absorption (SEIRA) techniques take advantage of these enhanced light-matter interactions to improve detection sensitivity [121,122].

The SINS response from the tip, antenna, and molecular vibration offers a means to go beyond SEIRA, taking advantage of the strong coupling within the resulting coupled dual-resonator system. Fig. 13 shows spatio-spectrally resolved SINS measurements of a poly(methyl methacrylate) (PMMA) thin film coated nanowire antennas with resonances near the C=O stretch (1775 cm^{-1}) of the PMMA [106]. In this example, coupling and energy transfer are measured through the spectrally resolved SINS signal from the nanotip, which also serves as an active and perturbative optical element, modifying the relative strengths of the different vibrational excitation pathways through 3D positioning relative to the nanowire. Both the nanotip and nanowire couple to far-field illumination, enabling the excitation of far-field forbidden nanowire overtone modes (dark modes). Furthermore, quantum interference between nanowire and nanotip excitation of the molecular vibrations leads to either peaks or spectral holes at the frequency of the molecular vibration. Drawing upon the plasmonic analogues of electromagnetically induced transparency (EIT) and electromagnetically induced absorption (EIA), this behavior can be modeled as classical electromagnetically induced scattering (EIS). These results demonstrate the ability to measure and modify plasmonic antenna responses coupled to molecular vibrations, enabled by the combined tip-enhanced near-field control and spectral bandwidth unique to SINS.

6.5. Quantum materials

With ultrabroadband coverage into the mid-to far-IR, SINS provides unique spectroscopic access to Drude conductivity, phonons, low-energy intra- and interband transitions, and surface polaritons in solid state systems. The sensitivity of SINS is high enough to discriminate, e.g., small changes in the local free carrier concentration associated with defects, doping, impurities, and layer thickness [123,124]. In an example combining optical, X-ray, and electron probes, SINS was used to investigate the electronic heterogeneities in topological insulator (TI) and thermoelectric materials Bi_2Se_3 and Sb_2Te_3 in a multimodal atomic-to-mesoscale resolution imaging study [125]. From the broadband SINS spectra and subsequent modeling of the tip-sample scattering response, the Drude free carrier concentration was extracted from several locations of the heterogeneous optical response in TI nanocrystals. Ultrahigh resolution elemental probes, including energy-dispersive X-ray spectroscopy (EDX) and transmission electron microscopy (TEM), were used to associate these optical inhomogeneities with the distribution and tuning of specific defects during the nanocrystal nucleation and growth stages. Linking optical heterogeneities to spatial variations in carrier concentration (likely due to defect distribution), as enabled by the broadband SINS response, contradicts recent claims of observations of SPPs in related Bi_2Te_3 nanoplatelets [126].

6.6. Phase-change materials

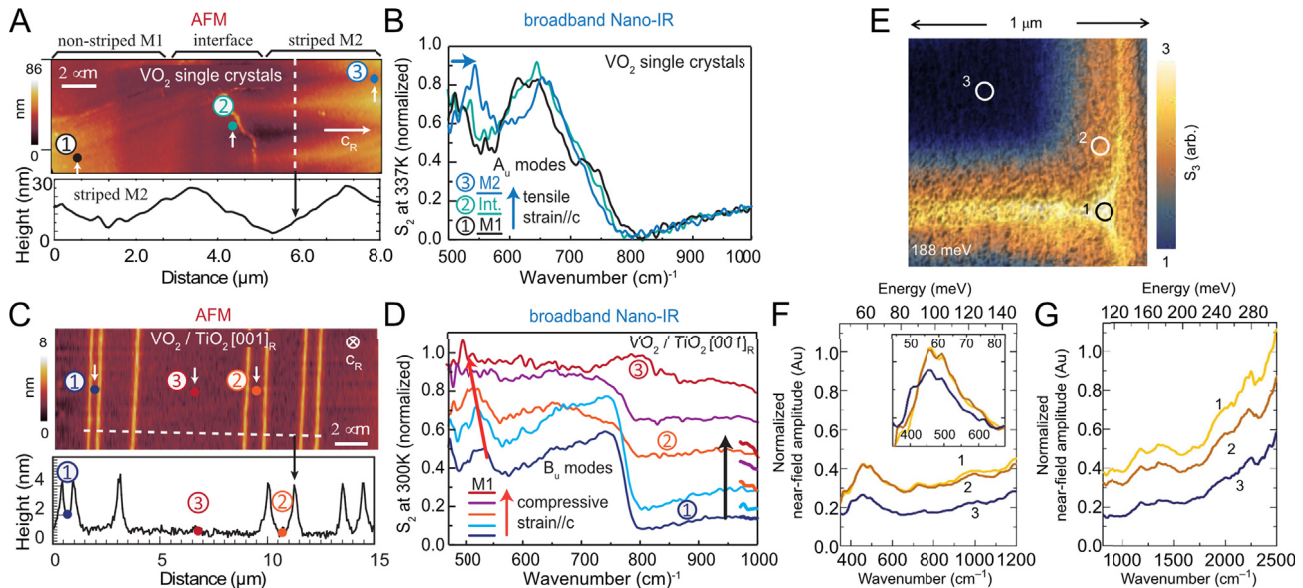Strain is an important parameter in condensed matter systems

Fig. 14. Phase transitions in the correlated materials VO$_2$ and SmS. (A) Top: AFM topography of an M1-M2 interface in a VO$_2$ single crystal at 337 K; bottom: AFM line scan of the striped M2 phase (along the white dashed line in the top panel). (B) Normalized SINS amplitude spectra at different locations corresponding to the spots indicated by the short white arrows in A. (C) Top: AFM topography of a 100-nm VO$_2$/TiO$_2$ [001]$_R$ film at room temperature. Bottom: AFM line scans of the buckles and the microbeams (along white dashed line in the top panel). (D) Normalized SINS amplitude spectra taken at the center of the microbeams with different beam widths. Three out of the five representative spectra are taken at the probe spots indicated by the short white arrows in C. For clarity, the curves in D are shifted vertically. The original positions of each curve are indicated at the high-frequency end of the same panel. (E) Near-field amplitude image of SmS at 188 meV (1515 cm^{-1}) and 295 K for a 1 μm^2 region showing contrast between the conductive patterned area (gold) and unpatterned semiconducting area (blue). Three locations are marked in the image, indicating semimetal (1), transition (2), and semiconducting (3) regions. Broadband near-field spectroscopy (normalized to a gold thin film) at 295 K is shown in F and G, for the locations specified in E. The exciton peak at 58 meV (468 cm^{-1}) is observable in all three regions. The inset in F, shows the exciton peaks with the background removed to highlight the slight frequency shift with applied pressure. Figures adapted with permission from Ref. [134,136]. (For interpretation of the references to color in this figure legend, the reader is referred to the Web version of this article.)

that can be used to modify the mechanical, electrical, and optical properties of a material and cause phase transitions in some materials. While many of these intrinsic properties can be observed macroscopically, strain acts locally and manifests itself in nanoscale heterogeneities. Infrared spectroscopy has long been used to determine the structure and electronic properties of materials, due to its extreme sensitivity to molecular and lattice vibrations, as well as low-energy electronic excitations. Extending earlier studies using laser-based s-SNOM [127–133], SINS, with its nanoscopic spatial resolution, has been used to study localized strain in a variety of phase-change materials, including vanadium dioxide (VO$_2$), samarium monosulfide (SmS), and calcium ruthenate (Ca$_2$RuO$_4$) [134–137].

For example, Fig. 14A–D shows SINS and laser-based s-SNOM measurements of vanadium dioxide (VO$_2$) microcrystals and oriented thin films [134]. The spectroscopic signatures of the phonon modes in VO$_2$ reveal lattice and electronic changes during phase transitions caused by temperature and/or strain. In the bulk single crystal, the IR active phonon responses of the M1 and M2 insulating phases were measured at three adjacent locations across the M1-M2 interface at 337 K. When going through the M1 to M2 phase transition, a blue shift of the ~520-cm^{-1} phonon (A$_u$ mode) peak was observed, indicative of tensile strain along the c_R axis. Similarly, in VO$_2$/TiO$_2$ [001]$_R$ films, a red shift of the M1 phonon ~540 cm^{-1} (B$_u$ mode) was observed, indicative of compressive strain along the c_R axis.

In another study, SINS was used to characterize the different phases of the strongly correlated heavy fermion system SmS [136]. SmS undergoes a semiconductor-to-semimetal phase transition at modest pressures (6.5 kbar), involving broad spectral weight redistribution within the 5d and 4f electron system. Contact-mode AFM was used to apply pressure to induce the local phase transition and subsequent SINS measurements probed the nanoscale phase separation. Fig. 14E shows a near-field amplitude image at 1515 cm^{-1} of three different regions of SmS of varying applied strain, with the dark region corresponding to the semiconducting phase, while the areas of higher signal indicate the semimetal phase and an intermediate transition region. SINS spectra of the respective regions are shown in Fig. 14F and G. In the FIR region, a peak at 468 cm^{-1} is attributable to an exciton near the indirect bandgap of SmS (~700 cm^{-1}), while the upward slope indicates the onset of the 4f^6-5d t$_{2g}$ absorption edge. The slight blueshift of the exciton peak in the lithographically strained regions is caused by lowering the 5d t^{2g} band and subsequent transfer of 4f electrons into the hybridized state, increasing the baseline reflectivity. This example highlights the simultaneous spectroscopic access to the indirect gap, exciton, and phonon resonances on the nanoscale in a quantum material using SINS.

6.7. Plasmon and phonon polaritons

Surface polaritons in solids are quasiparticles resulting from strong coupling of photons with collective modes in a crystal, such as plasmons in conductors or optical phonons in polar crystals, that have negative real parts of the dielectric function [33,138]. In s-SNOM, the large near-field momentum provided by the spatial field localization at the apex of the AFM tip is sufficient to optically excite these surface modes, as was demonstrated with surface plasmon polaritons (SPPs) in graphene [139–141] and surface phonon polaritons (SPhPs) in hexagonal boron nitride (hBN) [53], using laser-based s-SNOM nano-imaging. Unlike plasmon polaritons that usually span a very broad energy range, SPhPs provide a spectrally selective response associated with optical phonon modes. The initially tip-excited SPP or SPhP surface waves propagate radially outward from the near-apex launched region along the sample

surface until they reach the edge of the material or a grain boundary where the waves are reflected. The back-reflected waves interfere with the excitation field at the tip, causing an oscillation in the detected tip-scattered near-field light as a function of the distance from the edge to the tip, which can be modeled as a surface interferometer [141].

The large spectral bandwidth of the synchrotron source was exploited to simultaneously measure the two hBN Reststrahlen bands, the out-of-plane (~780 cm^{-1}) and in-plane (~1370 cm^{-1}) bands, both of which have the ability to support SPhPs [105]. Fig. 15 shows a SINS amplitude spatio-spectral linescan perpendicular to the edge of a 147 nm thick hBN flake, demonstrating a strong SPhP response in the higher frequency in-plane mode and a relatively weaker response in the lower-frequency out-of-plane mode. Although both modes show a strong SPhP wavelength dependence on excitation frequency, the sign of the dependence is reversed, which is consistent with the fact that the lower-frequency mode is a Type I hyperbolic mode and the upper-frequency mode is a Type II hyperbolic mode [142]. For the upper frequency mode near 1370 cm^{-1}, the main interference peak starts at high frequency near 1600 cm^{-1} at the edge of the flake and progressively red shifts
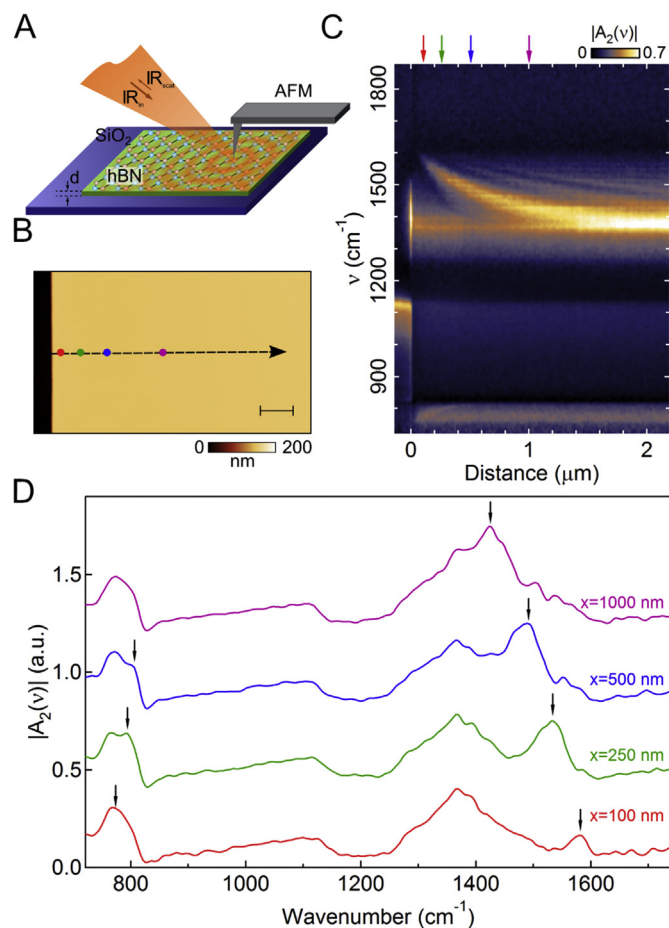

Fig. 15. hBN phonon polaritons. (A) Schematic illustrating phonon polaritons (PhP) propagation on hexagonal boron nitride (hBN) flakes. (B) Topography of d = 147 nm thick hBN flake with scale bar of 300 nm. (C) Spatio-spectral SINS |A$_2$($\bar{v}$)|, amplitude linescan along the black arrow indicated in B. covering both the hBN in-plane (~1370 cm^{-1}) and out-of-plane (~780 cm^{-1}) phonon modes, as well as the SiO$_2$ substrate (1130 cm^{-1}). (D) Representative |A$_2$($\bar{v}$)|, spectra at the locations of the colored circles in B and the colored arrows in C. The black arrows indicate spectral features caused by the interference of the forward and back-reflected PhP waves. Figure adapted with permission from Ref. [105].

toward 1370 cm^{-1} as the tip moves further from the edge, indicating an increase in SPhP wavelength with decreasing excitation frequency. For the lower-frequency mode near 780 cm^{-1}, the main interference peak starts at low frequency near 780 cm^{-1} at the hBN edge and blue shifts toward 820 cm^{-1} as the tip moves further from the edge, indicating an increase in SPhP wavelength with increased excitation frequency.

With graphene, a new generation of 2D optoelectronic materials can be envisioned by virtue of its inherently tunable IR and THz plasmonic response, though it is extremely sensitive to defects and coupling to the underlying substrate. Previous monochromatic IR s-SNOM nano-imaging studies demonstrated the observation of an electrically tunable plasmonic response in graphene nano-structures [139–141] where the plasmon wavelength is controlled by an externally applied gate voltage. More recently, the full voltage-dependent broadband nano-spectroscopic plasmonic response in pristine monolayer graphene flakes was probed with SINS [2]. Upon application of negative bias voltages, the SINS amplitude and phase responses were significantly enhanced (Fig. 16A and B red and blue shaded curves, respectively), whereas for high positive voltages, nearly full suppression was observed, approaching the intrinsic response of the underlying SiO$_2$ (black curve). This behavior is consistent with gate tuning of the Drude free carrier response superimposed with the SPP absorption in graphene. The spectral behavior and enhancement near the SiO$_2$ resonances indicate a hybridization and strong coupling between graphene SPPs and the substrate surface phonons. A spatio-spectral linescan across the edge of the graphene/SiO$_2$ device reveals the nanoscale heterogeneity of the SPP response (Fig. 16D). The SPP dispersion, as a function of energy, can readily be observed near the graphene interface, with the polariton wavelength determined by the distance of the modulated near-field amplitude and phase from the edge. The observation of only a single polariton branch is likely due to a strong damping of the plasmons. As shown in Fig. 16C, the appearance of a single polariton branch is common for graphene on SiO$_2$ not encapsulated in hBN because of a high density of charged impurity scatterers [143]. This direct nano-spectroscopic visualization of the coupled plasmon-phonon dispersion using SINS spans a spectral range four times as large as previous s-SNOM work on graphene plasmons [144], covering multiple coupled substrate phonon resonances, including the lower FIR plasmonic branch of graphene.

SINS has also been used to explore hybrid hyperbolic plasmon-phonon-polariton (HP^3) modes in graphene, hBN, and SiO$_2$ heterostructures [80,145]. The ability to access both Reststrahlen bands of hBN simultaneously with broadband synchrotron light highlights the differences in behavior between the type I and type II HP^3 bands over air, SiO$_2$, and Au substrates and their respective interfaces as illustrated in Fig. 17A. Tuning the applied bias voltage caused a strong modulation of the type I bands from coupling to Dirac plasmons in the graphene surface layer. Furthermore, intensity variations were observed in a continuous region of the top graphene/hBN layers (Fig. 17B) caused by the underlying air-Au metasurface, reminiscent of HP^3 propagation and reflection at an interface. The effect is strongest for the type I bands, which possess an out-of-plane polarization, because the different mode structure in the G-hBN/air and the G-hBN/Au regions of the waveguide impose an asymmetry for the power flow of the HP^3 modes across the junction between the two regions. This mechanism represents a rectifying diode behavior for the HP^3 modes, demonstrating unidirectional control of polariton propagation in graphene/hBN heterostructures.

Plasmon-phonon coupling has been explored in other 2D materials, including talc, which is an abundant, naturally occurring magnesium silicate mineral. In graphene-talc heterostructures (Fig. 17C), a strong enhancement of the out-of-plane mode at 1025 cm^{-1} was seen, as shown in Fig. 17D [107]. This enhancement was suppressed with an applied gate voltage that tuned the carrier
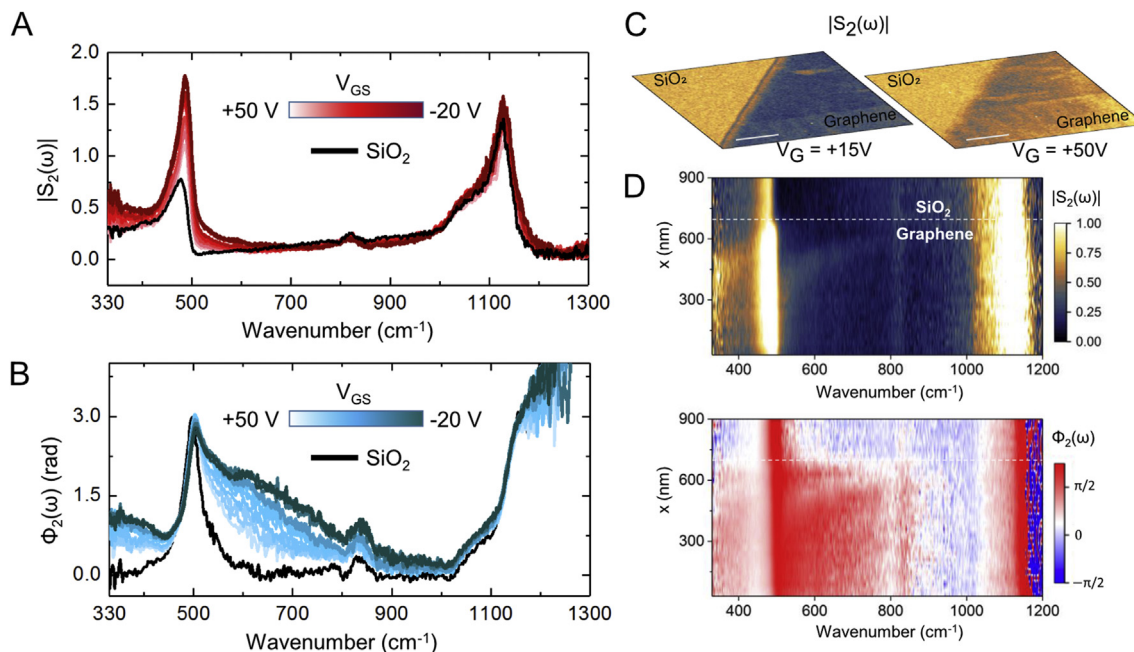

Fig. 16. Gate tuning of graphene devices. (A) SINS amplitude |S$_2$(ω)| (red shaded curves) and (B) phase Φ$_2$(ω) (blue shaded curves) for a functional graphene device on SiO$_2$ (black line), showing modulation of free carrier Drude response and plasmon absorption in graphene as a function of gate voltage. (C) SINS nanoimaging of graphene/SiO$_2$ interface for highly doped (V$_{GS}$ = +15 V, left) and low-doped (V$_{GS}$ = +50 V, right) graphene. Scale bar is 1 μm. (D) SINS spatio-spectral line scan (top: amplitude, bottom: phase) across doped-graphene/SiO$_2$ boundary, demonstrating nanometer broadband spectroscopic access to far-IR surface plasmon polariton (SPP) waves in graphene down to 320 cm^{-1}. The SPP dispersion as a function of energy can be observed directly near the graphene edge, where reflected surface waves constructively interfere with those launched from the AFM tip. Figure adapted with permission from Ref. [2]. (For interpretation of the references to color in this figure legend, the reader is referred to the Web version of this article.)
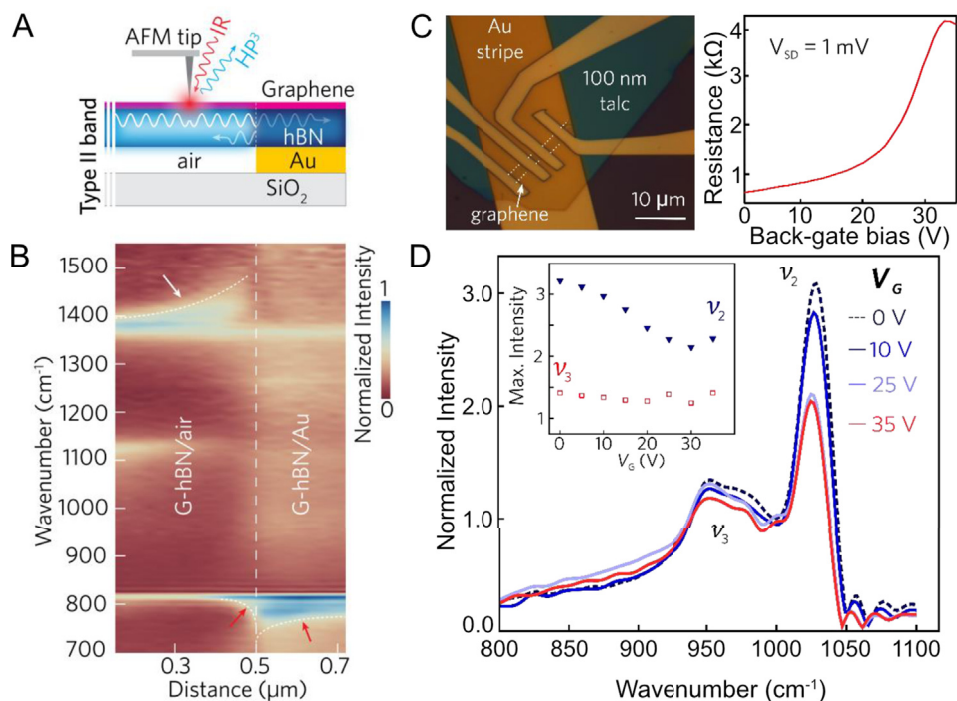
Fig. 17. (A) Schematics of polaritonic wave propagation near the graphene hBN/air and graphene-hBN/Au interface. (B) Spectral linescan, for zero gate voltage, across G-hBN/(air−Au) interface with regions of amplitude depletion or increase for the type I (on Au side) and type II (on air side) modes, as indicated by arrows. (C) (left) Optical image of graphene-talc/Au heterostructure with white dashed lines delimitating the graphene conducting channel. The talc thickness is 100 nm and scale bar represents 10 μm. (right) Resistance as a function of back-gate voltage (VG) for V_{SD} = 1 mV. (D) SINS point-spectra for the graphene-talc/Au heterostructure for selected gate bias. (inset) Maxima intensities of the SINS point-spectra for all gating measurements, demonstrating the gate tunability of the plasmon-phonon polaritons coupling between graphene and talc. Figures adapted with permission from Ref. [80,145], and [107].

density in the graphene and did not affect the lower energy in-plane vibration at 960 cm^{-1}. As with the case in graphene/SiO$_2$, this behavior is consistent with a high density of holes in the graphene strongly interacting with the out-of-plane vibrations in the talc substrate. The strong enhancement and slight blueshift of the 1025 cm^{-1} peak results from a plasmon-phonon coupling interaction that is tunable with gate voltage. These results suggest that talc and its 2D heterostructures, with strong responses in the mid- and far-infrared, have potential applications for low-cost nanophotonic devices.

7. Perspective

7.1. Source improvements

Coupling synchrotron infrared light with *s*-SNOM has made it possible to perform broadband spectroscopy spanning the far-IR and mid-IR (330 cm^{-1} − 4000 cm^{-1}) with a spatial resolution only limited by the tip radius (typically <25 nm). Single point spectra to full spatio-spectral images can be acquired with acquisition times that vary depending on the strength of the IR response of the sample material, spectral region, field of view, and spectral resolution of the measurement. At the ALS, a noise floor of <1° peak-to-peak can be achieved on gold reference samples for SINS 2nd harmonic phase signals in the 900-2000 cm^{-1} range. Thus, for samples with large IR-active dipole moments that couple effectively to the IR near-field of the tip, such as phonon polariton modes of hBN, spectra can be acquired with signal-to-noise ratios (SNR) greater than 30 with 8 cm^{-1} spectral resolution in as little as 1−2 min.

However, equivalent SNRs on samples without a high dielectric supporting substrate and with only moderate dipole moments,

such as the molecular amide I mode in proteins, may require acquisition times of 10 min or more. These long measurement times for even single point spectra currently limit the ability of routine collection of full hyperspectral images, in which high-spectral resolution data are acquired at each pixel of an image. Spectra can be acquired more rapidly with lower spectral resolution or SNR, but to realize the full potential of IR nano-spectroscopic imaging, the SNR must be improved and acquisition times reduced.

Increasing the spectral irradiance of the source is one obvious solution to increase the SNR of SINS. With integrated power levels of typically less than 2 mW in the mid-IR range, synchrotron IR light is well below the thermal damage threshold of most sample materials, even when focused to the diffraction-limit. Unfortunately, increasing the spectral irradiance by simply increasing the synchrotron ring current is generally not practicable because synchrotrons usually operate at the highest current technologically possible, which is limited by the thermal loading of optics, RF power, and electron beam stability. This approach towards higher IR power output could be achieved by designing and building a storage ring specifically optimized for producing infrared light. A lower electron-energy ring could operate at higher ring currents with lower thermal loads while still providing a diffraction limited source for infrared light. However, even such an approach is likely to improve the spectral irradiance only by a factor of 2−4. A more intriguing possibility is a dedicated storage ring with an altered electron bunch length to optimize the production of coherent synchrotron radiation (CSR) in the far-IR. Such a facility was proposed [146] and has the possibility to increase the flux of light below 100 cm^{-1} by more than six orders of magnitude compared to what is available at modern X-ray synchrotrons. Other proposed upgrades, such as the VSR upgrade project of BESSY II, have the potential to increase CSR power and spectral range, while

simultaneously maintaining conditions suitable for standard synchrotron experiments [147].

An alternative approach to increasing the spectral irradiance of the source is to improve the collection efficiency and focusing conditions of the IR beam. The total flux of an infrared beamline is proportional to the synchrotron ring current and the horizontal aperture of the beamline, which is practically limited by the physical constraints of the storage ring vacuum chamber and the dipole bend magnet. To increase the flux, most infrared beamlines maximize the horizontal collection aperture and use a combination of planar, toroidal, and elliptical mirrors to redirect and collimate the light from the synchrotron before coupling it into an experimental setup. However, the geometrical aberrations produced by the circular shape of the bending magnet source increase with the square of the horizontal beamline aperture. Because the photon source size is a convolution of the geometric aberrations, electron beam size, and diffraction limit, increasing the horizontal aperture larger than the natural opening angle θ_{nat}, can introduce large coma aberrations and reduce the ability to collimate or focus to a diffraction limited spot. Furthermore, as the horizontal aperture is increased, distortions in the vertical emission profile become more prevalent because of overlapping vertical emission produced at each point in the electron trajectory.

Aberration-free collection of synchrotron IR radiation is possible with appropriate beamline design using the combination of a cylindrical and a conical mirror [148–150]. This approach has been implemented at Beamline 2.4 of the ALS (USA) and in the IR1 infrared beamline at LNLS (Brazil), which was designed specifically for SINS measurements [82]. The geometric aberrations can also be corrected with a single mirror, as demonstrated at BL6B at UVSOR-II (Japan), which uses a specially-designed three dimensional extended "magic" mirror for the large 80(V) x 215(H) x mrad² collection angle of that beamline.

Beamline focusing can further be improved with the use of deformable mirrors to correct optical aberrations and achieve wavefront control of synchrotron IR radiation. The use of adaptive optics is well known in astronomy and optical imaging to correct for the aberrations due to Earth's atmosphere and to correct optic and sample aberrations, respectively [151]. If the optical aberrations of a beamline can be accurately measured, then a deformable mirror can be used to correct the optical systems statically or even dynamically, with feedback based on metrics derived from the s-SNOM spectral signal. An optimized wavefront will potentially improve the interferometric signal detection by providing a better spatial mode of the reference beam to interfere with the scattered light of the tip.

The above approaches aim to improve SINS SNR by increasing the spectral irradiance at the tip. Alternatively, the SNR can be improved by reducing the noise of the source. The primary noise sources for synchrotron radiation are temporal fluctuations caused by mechanical vibrations and electron orbit instabilities. Many synchrotrons are taking advantage of new accelerator designs and vacuum technologies to upgrade or build diffraction-limited storage rings, which will use smaller electron beams to generate X-rays with high coherence. Although these new storage rings will have smaller vacuum chambers that will complicate the extraction of IR radiation, they will by necessity require tighter control of the electron beam and mechanical components. Therefore, while diffraction-limited storage rings are unlikely to improve the SINS signal, they have the prospect of increasing SINS SNR by reducing the noise of the source.

7.2. Tip engineering

The AFM tip is a critical component of an s-SNOM experiment. As an optical antenna, the tip receives the propagating incident far-field radiation, localizes it in a nanoscopic region, and couples it in the near-field to the sample [152]. The tip also performs the reciprocal process, coupling the near-field light from the sample to the far-field, which is ultimately measured by an IR detector. Thus, to fully optimize s-SNOM sensitivity, careful consideration should be given to the optical antenna response of the tip, in terms of its antenna resonance, Ohmic losses, and impedance/electromagnetic local density of states [152].

Despite the need to improve the optical antenna properties of the tip, most s-SNOM experiments performed to date use metal-coated (e.g. PtIr, Au, or PtSi) silicon AFM tips that have not been optimized for s-SNOM measurements in any particular way. These commonly used tips are mass produced with standard lithographic techniques and are commercially available at modest costs. The low aspect ratios of these tips lead to broad antenna resonances, which enable coupling of infrared light across broad spectral ranges and is advantageous for SINS measurements that span the entire IR region. Although the tip response is broad, most commercially available tips have a decreased enhancement at higher frequencies, such that near-field enhancement can be several times less at frequencies above 3000 cm^{-1} compared to 1000 cm^{-1}, as observed both theoretically and experimentally [76,153]. These commonly used metal-coated tips are well-suited to a broad range of systems, but they offer only modest performance compared with an optimized tuning of the antenna response of the tip.

Many applications could benefit from the increased sensitivity and spatial resolution offered by tips with engineered antenna resonances. Several measurements have been performed with elongated antenna probes, fabricated with focused ion beam (FIB) processes, that provide near-field enhancement of nearly an order of magnitude compared to conventional AFM tips [153–155]. These elongated tips could be particularly beneficial for the far-IR/THz regime where the longer shank lengths are required to effectively couple and localize the long wavelengths. The tip apex also determines the ultimate spatial resolution of the technique. While most commercial metal coated AFM tips have apexes <25 nm, sharper tips offer the prospect of improved spatial resolution, as recently demonstrated using a FIB modified tungsten tip to achieve a spatial resolution of 5 nm [156].

7.3. Algorithm development

In addition to improving the source spectral irradiance, focusing, and tip to far-field coupling, hyperspectral imaging acquisition times can be improved by implementing computational techniques, such as compressive sensing and matrix completion, as established in other fields of imaging science. In the case of compressed sensing, the complete reconstruction of a subsampled dataset can be achieved provided that the global dataset has a sparse representation in a suitably chosen basis. This technique was adapted to SINS and simulated recovering complete interferograms at sub-Nyquist sampling rates and spectral features, demonstrating an improvement in spectroscopic acquisition by reducing the number of measured data points by a factor of ~10 [157]. In this example, the redundancy that is being exploited is along the reference arm mirror position during a spectral scan. Most samples have additional redundancy in the spatial domain that could enable further data reduction. One method of incorporating this additional redundancy is to apply compressed sensing techniques to the spatial domain by exploiting sparsity in, for example, the curvelet

or wavelet domain. Alternatively, filtering the basis functions based on a global requirement of 50% non-sparsity per basis function was shown.

An additional and generalizable method to incorporate spatial redundancy and spectral sparsity is matrix completion, which achieves a reconstructed image by incorporating prior knowledge about the sample. Once a subset of data is chosen to be measured, the positions of the reference arm and sample stage are linked by the experimental trajectory to collect the subsampled data points, which can be further optimized for acquisition speed [158]. This experiment would then move the sample and the reference arm mirror simultaneously in the 3D configurational space.

The methods mentioned above are static pre-experiment determinations of subsampled datasets. Algorithms can additionally be used in which the size of the spatio-spectral data set is refined during acquisition in response to the ongoing measurement. This adaptive data acquisition allows for flexible sampling with more refined data points in regions of interest determined by additions to the previously acquired data, rather than having a fixed sampling matrix that would spend an unnecessarily long time in areas with high redundancy. Implementing full spatio-spectral prior knowledge algorithms requires, at a minimum, precise control and high position accuracy of the interferometric reference arm or sample position. Implementing compressive sensing algorithms for maximal acquisition speed along only one dimension should be done along the dimension with minimal "dead time" between sampled data points. Although one of the primary advantages of SINS is the ability to probe the full-infrared range simultaneously, many applications require measuring only a few selected resonances within the broader spectral range of the synchrotron. Another new spatio-spectral nano-imaging modality and data processing scheme was demonstrated where hyperspectral images were collected by transforming from the stationary frame into the rotating frame of the IR carrier frequency, which lowers the Nyquist cut-off frequency and decreases the number of necessary data points for spectral reconstruction [159]. With prior knowledge of

the electronic or vibrational resonances to be probed, a factor of 10 or more improvement in acquisition speed for chemical nano-imaging ultrathin protein sheets in a mollusk shell was achieved (Fig. 18).

7.4. Controlled environments

Although SINS provides many advantages due to its suitability for measurement under ambient conditions, a greater range of applications for materials science, biology, and chemistry is possible with the addition of variable sample temperature and environmental control with gas, vacuum, or liquid environments. In materials science, variable temperature cryogenic control down to few or even sub-Kelvin temperatures enables the exploration of nanoscale phenomena, e.g., as associated with phase transitions in quantum materials, heterogeneities of electronic or magnetic properties and their dependence on temperature, or bath coupling and loss of quantum coherence as relevant for quantum information science applications. In biological research, liquid environments enable biomolecular imaging in native hydrated states and *in vivo* measurements of living systems. In chemistry, variable gas/vapor phase control enables *in situ* measurements of catalytic reactions and, in combination with liquids, *in operando* probing of nanometer thin interfaces and interphases in electrochemical devices.

Currently, AFM techniques exist that can readily access all these desired experimental conditions. However, the combination of a cryogenic or in-liquid AFM with the necessary optical access and IR illumination provides additional technical challenges. For example, standard cryo-AFM designs with cold-shields often constrict free line of sight for tip-sample illumination with high numerical aperture (NA) optics. Nevertheless, several cryogenic *s*-SNOM instruments have been developed and operated successfully with laser based sources. Combining a microscope cryostat with a cryo-compatible AFM was the first proof of concept for *s*-SNOM operating under cryogenic and variable temperature (~20−500 K
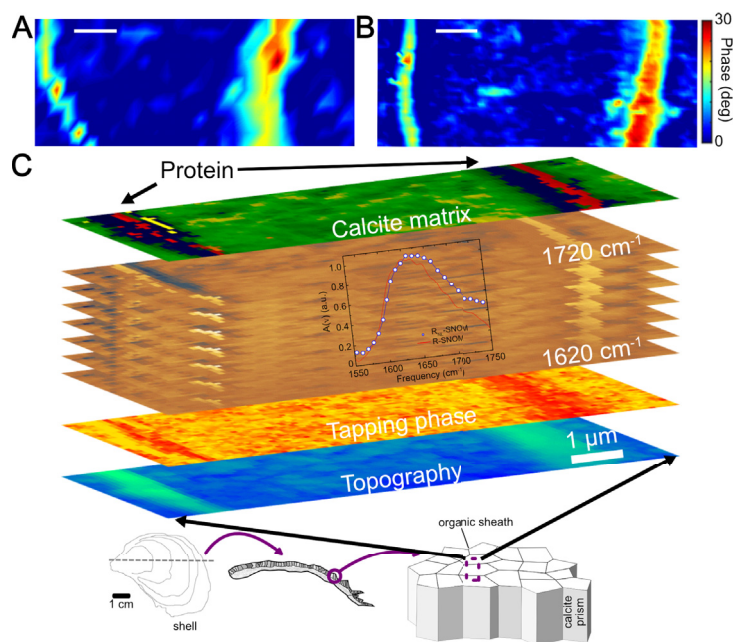
Fig. 18. Spatio-spectral nano-imaging in the rotating frame. (A) Conventional nano-FTIR spatio-spectral imaging and (B) rotating frame spatio-spectral imaging of protein sheets in an oyster shell. Both data sets acquired for the same measurement time, with rotating frame yielding significantly higher image content and simultaneous facile drift correction. Scale bar is 1 μm. (C) Correlative analysis (top) of chemical (middle) and mechanical (bottom) channels that together enable identification of long elusive protein layer in shell (illustration). Figure adapted with permission from Ref. [159].

compatible with possible extension to high magnetic fields up to 7 T) [160]. Further extension to the ultra-high vacuum (UHV, pressures below 10^{-9} mbar) was developed with variable temperature control, utilizing a sample heater and liquid helium cryostat to access sample temperatures from 20 to 450 K [161]. Recently, s-SNOM measurements were extended down to T = 5 K and were combined with a free electron laser (FEL) for narrowband, tunable radiation from the far-IR to the mid-IR [46]. The recent availability of commercial cryogenic s-SNOM nanoscopes further indicates that these types of instruments are not only feasible, but also practicable in a user environment that requires flexibility of samples and quick sample exchange to efficiently use allocated beamtime.

Liquid environments pose additional challenges for SINS measurements. Tip illumination is difficult because of the strong absorption of IR light by common liquids, such as water. For far-field measurements, solvent absorption can be overcome by maintaining a sufficiently thin liquid layer (typically less than 10 μm) to minimize the amount of IR absorption but still provide hydration and/or nutrient delivery. This approach has been achieved through a closed cell design with an appropriate thin spacer or through more advanced microfluidic channel techniques [63]. Performing conventional s-SNOM in this thin liquid regime is difficult because the liquid strongly damps the oscillatory motion of the AFM cantilever, reducing the effectiveness of high harmonic detection to remove far-field background contributions. A route around these technical challenges was demonstrated by encapsulating small amounts of water within graphene to enable s-SNOM measurements in ambient conditions [162]. In this approach, graphene functioned as an ultra-thin IR transparent "coverslip" by serving as an impermeable liquid barrier. This platform, as demonstrated, is limited to studies involving very small liquid volumes trapped under graphene and can lead to high hydrostatic pressures, which could affect native biomolecule conformation. The coverslip concept has been extended to larger liquid volumes through appropriate cell design, allowing ambient conditions on the probe side and bulk liquid conditions on the other side. Such a device enables exploration of biological systems in their native environments [163] and exploration of electrochemical properties at solid-liquid interfaces [164].

Another approach to minimize solvent absorption of IR light is through attenuated total reflectance (ATR) methods, in which infrared light is reflected off the surface of a high-index material (e.g. germanium, zinc selenide, diamond) via total internal reflection [165]. This mechanism results in an evanescent wave that only propagates a few hundred nanometers to a few microns into the sample, depending on the indices of refraction of the crystal and material, wavelength, and angle of incidence. Evanescent excitation in s-SNOM thus provides an alternative means for tip illumination that would enable a tip to be fully submerged in a liquid, thereby minimizing anharmonic distortions of the oscillatory tip-motion from surface tension. This approach is limited to thin samples and requires modifications to commercially available/standard s-SNOM instruments with top-down tip illumination. Nevertheless, the approach offers the potential to study various types of biological/chemical process in situ/in operando [166].

7.5. Extending toward the far-IR and THz

The far-IR region is rich with low-frequency phonon modes of many materials. However, few lasers suitable for s-SNOM can access the 10-600 cm^{-1} regime, particularly for broadband spectroscopy. As a consequence, the so-called THz gap is largely unexplored for IR s-SNOM measurements [167]. Synchrotron radiation extends to this region of the spectrum and appears to be well-suited for nanospectroscopy [2]. Spectra with synchrotron

light has been measured down to ~320 cm^{-1}, which is the low-frequency cutoff of Ge:Cu detectors. Detectors suitable for s-SNOM in the region below 300 cm^{-1} are scarce. The ideal detector for far-IR SINS would have high sensitivity (NEP≤1 pW/$\sqrt{Hz}$), broad spectral coverage (10 cm^{-1}-1000 cm^{-1}), and a high detection speed (>500 kHz) to respond to higher harmonics of force-modulation (~250 kHz) AFM tips. Composite silicon bolometers, which are typically used for conventional far-IR measurements, have the necessary sensitivity and bandwidth, but are exceedingly slow in their standard configuration with detection speeds of <1 kHz. With appropriate reduction in aperture and absorber size, combined with lower temperature operation, it may be possible to increase the speed of these detectors sufficiently [168]. Superconducting hot electron bolometers offer another possibility for this spectral range. These detectors are fast and broadband with coverage from 30 to 1000 cm^{-1}, but the sensitivity is limited to ~10 pW/$\sqrt{Hz}$, nearly 2 orders of magnitude worse than a bolometer.

With appropriate detectors, the far-IR region offers the possibility to explore other modes of synchrotron IR, namely coherent synchrotron radiation (CSR). As discussed above, CSR can be 7 to 9 orders of magnitude stronger than conventional single particle synchrotron emission. Because CSR is generated only when the electron bunch length is less than the wavelength of light, CSR is typically only present in the far-IR < 100 cm^{-1}. The BESSY II synchrotron in Germany can deliver up to 300 μW of CSR in the 3-33 cm^{-1} region, and has an upgrade path to further increase the power and spectral range through the use of superconducting bunch compression cavities [147]. CSR has also been generated at higher frequencies in so-called "laser-slicing" experiments, where a femtosecond laser is overlapped in space and time with an electron bunch, such that the electric field modulates the electron energy and effectively slices a hole in the electron bunch. In this case, the hole radiates CSR on the length scale of the femtosecond laser pulse up to ~300 cm^{-1} [169]. Thus far, these laser-slicing experiments have been performed with lasers operating with 1 kHz repetition rates, making them less suitable for s-SNOM measurements. However, these experiments have demonstrated the potential use of CSR at higher frequencies. Current accelerator source development has focused on free electron lasers with high repetition rates and extremely short pulses, which under the right circumstances have the potential for extending CSR to higher frequencies, perhaps into the mid-IR.

With additional detector and source development, the extension of s-SNOM into the far-IR with synchrotron infrared light will expand the measurement boundaries of materials physics, particularly if coupled with the cryogenic capabilities discussed above. By probing the low energy excitations of phonon modes, band gaps, and surface polaritons with precise temperature control, further explorations of novel correlated and phase-change materials will be enabled.

8. Summary

By combining synchrotron infrared radiation with near-field techniques, SINS improves the spatial resolution of IR microspectroscopy by 2-3 orders of magnitude, providing label-free, detailed chemical and physical information at the nanoscale with high sensitivity and simultaneous full-coverage of the mid-IR to far-IR. Although this powerful technique is just emerging, it already has been widely applied to various materials in a number of diverse scientific fields. Perhaps the most important advantage of SINS not yet emphasized is the user facility aspect, which makes nearfield IR widely available to researchers of all fields, such that subject matter experts can use the technique to address the most pressing

scientific questions in their field without the need to fund, develop, and maintain their own systems. The broad bandwidth of the source allows a high throughput of different samples that may have features of interest in different spectral regions, which in the case of a narrowband source could require a source change and/or realignment for optimal SNR. The spectrum of the synchrotron source and alignment is remarkably stable, such that long averages are possible. The development of SINS has revolutionized IR beamlines worldwide with several operating endstations at ALS (USA), MLS (Germany), and LNLS (Brazil) with many more endstations across the world currently under development.

This review of the development of SINS has been written with citations as comprehensive as possible and omissions unintended. SINS is the result of the convergence of several advances of near-field imaging and based on nearly 20 years of success in understanding and modeling. This progress was further enabled by its adoption across different disciplines for a wide range of applications. We anticipate that just as far-field and FTIR micro-spectroscopy have become established techniques, synchrotron based nano-spectroscopy will complement other table-top methods for nano-imaging and continue to contribute to the frontiers of nanoscale science.

Funding

Acknowledgements

References

[1] G. Herzberg, Molecular Spectra and Molecular Structure. Vol. 2: Infrared and Raman Spectra of Polyatomic Molecules, Van Nostrand, Reinhold, New York, 1945.

[2] O. Khatib, H.A. Bechtel, M.C. Martin, M.B. Raschke, G.L. Carr, Far infrared synchrotron near-field nanoimaging and nanospectroscopy, ACS Photonics 5 (2018) 2773–2779.

[3] R.G. Messerschmidt, M.A. Harthcock, IR Microspectroscopy Theory and Applications, Marcel Dekker, New York, 1988.

[4] I.W. Levin, R. Bhargava, Fourier transform infrared vibrational spectroscopic imaging: integrating microscopy and molecular recognition, Annu. Rev. Phys. Chem. (2005) 429–474.

[5] M. Minsky, Microscopy Apparatus, 1961. US Patent 3,013,467.

[6] M.J. Nasse, M.J. Walsh, E.C. Mattson, R. Reininger, A. Kajdacsy-Balla, V. Macias, R. Bhargava, C.J. Hirschmugl, High-resolution Fourier-transform infrared chemical imaging with multiple synchrotron beams, Nat. Methods 8 (2011) 413–416.

[7] E.C. Mattson, M.J. Nasse, M. Rak, K.M. Gough, C.J. Hirschmugl, Restoration and spectral recovery of mid-infrared chemical images, Anal. Chem. 84 (2012) 6173–6180.

[8] E. Stavitski, R.J. Smith, M.W. Bourassa, A.S. Acerbo, G.L. Carr, L.M. Miller, Dynamic full-field infrared imaging with multiple synchrotron beams, Anal. Chem. 85 (2013) 3599–3605.

[9] E.H. Synge, A suggested method for extending microscopic resolution into the ultra-microscopic region, The Lond., Edinb., Dublin Phil. Mag. J. Sci. 6 (1928) 356–362.

[10] E.A. Ash, G. Nicholls, Super-resolution aperture scanning microscope, Nature 237 (1972) 510–512.

[11] D.W. Pohl, W. Denk, M. Lanz, Optical stethoscopy - image recording with resolution lambda/20, Appl. Phys. Lett. 44 (1984) 651–653.

[12] E. Betzig, J.K. Trautman, T.D. Harris, J.S. Weiner, R.L. Kostelak, Breaking the diffraction barrier - optical microscopy on a nanometric scale, Science 251 (1991) 1468–1470.

[13] U. Durig, D.W. Pohl, F. Rohner, Near-field optical-scanning microscopy, J. Appl. Phys. 59 (1986) 3318–3327.

[14] B. Hecht, B. Sick, U.P. Wild, V. Deckert, R. Zenobi, O.J.F. Martin, D.W. Pohl, Scanning near-field optical microscopy with aperture probes: fundamentals and applications, J. Chem. Phys. 112 (2000) 7761–7774.

[15] J. Wessel, Surface-enhanced optical microscopy, J. Optic. Soc. Am. B-Opt. Phys. 2 (1985) 1538–1541.

[16] U.C. Fischer, D.W. Pohl, Observation of single-particle plasmons by near-field optical microscopy, Phys. Rev. Lett. 62 (1989) 458–461.

[17] Y. Inouye, S. Kawata, Near-field scanning optical microscope with a metallic probe tip, Optic Lett. 19 (1994) 159–161.

[18] F. Zenhausern, Y. Martin, H.K. Wickramasinghe, Scanning interferometric apertureless microscopy - optical imaging at 10 angstrom resolution, Science 269 (1995) 1083–1085.

[19] B. Knoll, F. Keilmann, Near-field probing of vibrational absorption for chemical microscopy, Nature 399 (1999) 134–137.

[20] M.B. Raschke, C. Lienau, Apertureless near-field optical microscopy: tip-sample coupling in elastic light scattering, Appl. Phys. Lett. 83 (2003) 5089–5091.

[21] T. Taubner, R. Hillenbrand, F. Keilmann, Nanoscale polymer recognition by spectral signature in scattering infrared near-field microscopy, Appl. Phys. Lett. 85 (2004) 5064.

[22] F. Keilmann, R. Hilenbrand, Near-field nanoscopy by elastic light scattering from a tip, in: D. Richards, A. Zayats (Eds.), Nano-optics and Near-Field Optical Microscopy, Artech House, Boston/London, 2009, pp. 235–266.

[23] J.M. Atkin, S. Berweger, A.C. Jones, M.B. Raschke, Nano-optical imaging and spectroscopy of order, phases, and domains in complex solids, Adv. Phys. 61 (2012) 745–842.

[24] E.A. Muller, B. Pollard, M.B. Raschke, Infrared chemical nano-imaging: accessing structure, coupling, and dynamics on molecular length scales, J. Phys. Chem. Lett. 6 (2015) 1275–1284.

[25] X. Chen, D. Hu, R. Mescall, G. You, D.N. Basov, Q. Dai, M. Liu, Modern scattering-type scanning near-field optical microscopy for advanced material research, Adv. Mater. 31 (2019) 1804774.

[26] A. Dazzi, R. Prazeres, E. Glotin, J.M. Ortega, Local infrared microspectroscopy with subwavelength spatial resolution with an atomic force microscope tip used as a photothermal sensor, Optic Lett. 30 (2005) 2388–2390.

[27] A. Centrone, Infrared imaging and spectroscopy beyond the diffraction limit, in: R.G. Cooks, J.E. Pemberton (Eds.), Annual Review of Analytical Chemistry, vol. 8, 2015, pp. 101–126.

[28] A. Dazzi, C.B. Prater, AFM-IR: Technology and applications in nanoscale infrared spectroscopy and chemical imaging, Chem. Rev. 117 (2017) 5146–5173.

[29] D. Nowak, W. Morrison, H.K. Wickramasinghe, J. Jahng, E. Potma, L. Wan, R. Ruiz, T.R. Albrecht, K. Schmidt, J. Frommer, D.P. Sanders, S. Park, Nanoscale chemical imaging by photoinduced force microscopy, Sci. Adv. 2 (2016), e1501571.

[30] B.T. O'Callahan, J. Yan, F. Menges, E.A. Muller, M.B. Raschke, Photoinduced tip-sample forces for chemical nanoimaging and spectroscopy, Nano Lett. 18 (2018) 5499–5505.

[31] J. Jahng, E.O. Potma, E.S. Lee, Tip-enhanced thermal expansion force for nanoscale chemical imaging and spectroscopy in photoinduced force microscopy, Anal. Chem. 90 (2018) 11054–11061.

[32] J. Jahng, D.A. Fishman, S. Park, D.B. Nowak, W.A. Morrison, H.K. Wickramasinghe, E.O. Potma, Linear and nonlinear optical spectroscopy at the nanoscale with photoinduced force microscopy, Acc. Chem. Res. 48 (2015) 2671–2679.

[33] I.D. Barcelos, H.A. Bechtel, C.J.S. de Matos, D.A. Bahamon, B. Kaestner, F.C.B. Maia, R.O. Freitas, Probing polaritons in 2D materials with synchrotron infrared nanospectroscopy, Adv. Optic. Mater. 8 (2020) 1901091.

[34] W.D. Duncan, G.P. Williams, Infrared synchrotron radiation from electron storage rings, Appl. Optic. 22 (1983) 2914–2923.

[35] K.D. Moller, D.P. Siddons, C.J. Hirschmugl, D. Scardino, P. Petrone, D. Carlson, G.P. Williams, 2-mirror wave-front-dividing interferometer for infrared synchrotron radiation, Appl. Optic. 30 (1991) 4297–4301.

[36] M. Abo-Bakr, J. Feikes, K. Holldack, P. Kuske, W.B. Peatman, U. Schade, G. Wustefeld, H.W. Hubers, Brilliant, coherent far-infrared (THz) synchrotron radiation, Phys. Rev. Lett. 90 (2003), 094801.

[37] J. Barros, C. Evain, L. Manceron, J.B. Brubach, M.A. Tordeux, P. Brunelle, L. Nadolski, A. Loulergue, M.E. Couprie, S. Bielawski, C. Szwaj, P. Roy, Coherent synchrotron radiation for broadband terahertz spectroscopy, Rev. Sci. Instrum. 84 (2013), 033102.

[38] C. Steier, B. Bailey, K. Baptiste, W. Barry, A. Biocca, W. Byrne, M. Chin, R. Donahue, R. Duarte, M. Fahmie, B. Gath, S. Jacobson, J. Julian, J.Y. Jung, S. Kwiatkowski, S. Marks, R. Mueller, H. Nishimura, J. Oneill, S. Prestemon, D. Robin, S. Rossi, F. Sannibale, T. Scarvie, R. Schlueter, D. Shuman, G. Stover, C. Timossi, T. Warwick, J. Weber, E. Williams, Status of the top-off upgrade of the ALS, in: 2007 IEEE Particle Accelerator Conference, 2007, pp. 1197–1199.

[39] F. Huth, M. Schnell, J. Wittborn, N. Ocelic, R. Hillenbrand, Infrared-spectroscopic nanoimaging with a thermal source, Nat. Mater. 10 (2011) 352–356.

[40] B.T. O'Callahan, W.E. Lewis, S. Mobius, J.C. Stanley, E.A. Muller, M.B. Raschke, Broadband infrared vibrational nano-spectroscopy using thermal blackbody radiation, Optics Express 23 (2015) 32063–32074.

[41] D.J. Lahneman, T.J. Huffman, P. Xu, S.L. Wang, T. Grogan, M.M. Qazilbash, Broadband near-field infrared spectroscopy with a high temperature plasma light source, Optics Express 25 (2017) 20421–20430.

[42] M. Wagner, D.S. Jakob, S. Horne, H. Mittel, S. Osechinskiy, C. Phillips, G.C. Walker, C.M. Su, X.J.G. Xu, Ultrabroadband nanospectroscopy with a laser-driven plasma source, ACS Photonics 5 (2018) 1467–1475.

[43] N. Ocelic, A. Huber, R. Hillenbrand, Pseudoheterodyne detection for background-free near-field spectroscopy, Appl. Phys. Lett. 89 (2006) 101124.

[44] S. Berweger, D.M. Nguyen, E.A. Muller, H.A. Bechtel, T.T. Perkins, M.B. Raschke, Nano-chemical infrared imaging of membrane proteins in lipid bilayers, J. Am. Chem. Soc. 135 (2013) 18292–18295.

[45] F. Kuschewski, H.G. von Ribbeck, J. Doering, S. Winnerl, L.M. Eng, S.C. Kehr, Narrow-band near-field nanoscopy in the spectral range from 1.3 to 8.5 THz, Appl. Phys. Lett. 108 (2016) 113102.

[46] D. Lang, J. Doring, T. Norenberg, A. Butykai, I. Kezsmarki, H. Schneider, S. Winnerl, M. Helm, S.C. Kehr, L.M. Eng, Infrared nanoscopy down to liquid helium temperatures, Rev. Sci. Instrum. 89 (2018), 033702.

[47] F. Huth, A. Govyadinov, S. Amarie, W. Nuansing, F. Keilmann, R. Hilenbrand, Nano-FTIR absorption spectroscopy of molecular fingerprints at 20 nm spatial resolution, Nano Lett. 12 (2012) 3973–3978.

[48] R. Hegenbarth, A. Steinmann, S. Mastel, S. Amarie, A.J. Huber, R. Hillenbrand, S.Y. Sarkisov, H. Giessen, High-power femtosecond mid-IR sources for s-SNOM applications, J. Optic. 16 (2014) 7094003.

[49] X.G. Xu, M. Rang, I.M. Craig, M.B. Raschke, Pushing the sample-size limit of infrared vibrational nanospectroscopy: from monolayer toward single molecule sensitivity, J. Phys. Chem. Lett. 3 (2012) 1836–1841.

[50] I. Amenabar, S. Poly, W. Nuansing, E.H. Hubrich, A.A. Govyadinov, F. Huth, R. Krutokhvostov, L. Zhang, M. Knez, J. Heberle, A.M. Bittner, R. Hillenbrand, Structural analysis and mapping of individual protein complexes by infrared nanospectroscopy, Nat. Commun. 4 (2013) 2890.

[51] S. Bensmann, F. Gaussmann, M. Lewin, J. Wueppen, S. Nyga, C. Janzen, B. Jungbluth, T. Taubner, Near-field imaging and spectroscopy of locally strained GaN using an IR broadband laser, Optics Express 22 (2014) 22369–22381.

[52] S. Amarie, P. Zaslansky, Y. Kajihara, E. Griesshaber, W.W. Schmahl, F. Keilmann, Nano-FTIR chemical mapping of minerals in biological materials, Beilstein J. Nanotechnol. 3 (2012) 312–323.

[53] S. Dai, Z. Fei, Q. Ma, A.S. Rodin, M. Wagner, A.S. McLeod, M.K. Liu, W. Gannett, W. Regan, K. Watanabe, T. Taniguchi, M. Thiemens, G. Dominguez, A.H. Castro Neto, A. Zettl, F. Keilmann, P. Jarillo-Herrero, M.M. Fogler, D.N. Basov, Tunable phonon polaritons in atomically thin van der Waals crystals of boron nitride, Science 343 (2014) 1125–1129.

[54] G. Dominguez, A.S. McLeod, Z. Gainsforth, P. Kelly, H.A. Bechtel, F. Keilmann, A. Westphal, M. Thiemens, D.N. Basov, Nanoscale infrared spectroscopy as a non-destructive probe of extraterrestrial samples, Nat. Commun. 5 (2014) 5445.

[55] I.T. Lucas, A.S. McLeod, J.S. Syzdek, D.S. Middlemiss, C.P. Grey, D.N. Basov, R. Kostecki, IR near-field spectroscopy and imaging of single Li_xFePO_4 microcrystals, Nano Lett. 15 (2015) 1–7.

[56] C. Calabrese, A.M. Stingel, L. Shen, P.B. Petersen, Ultrafast continuum mid-infrared spectroscopy: probing the entire vibrational spectrum in a single laser shot with femtosecond time resolution, Optic Lett. 37 (2012) 2265–2267.

[57] R. Huber, A. Brodschelm, F. Tauser, A. Leitenstorfer, Generation and field-resolved detection of femtosecond electromagnetic pulses tunable up to 41 THz, Appl. Phys. Lett. 76 (2000) 3191–3193.

[58] Stevenso Jr., H. Ellis, R. Bartlett, Synchrotron radiation as an infrared source, Appl. Optic. 12 (1973) 2884–2889.

[59] G.L. Carr, J.A. Reffner, G.P. Williams, Performance of an infrared microspectrometer at the NSLS, Rev. Sci. Instrum. 66 (1995) 1490–1492.

[60] J.A. Reffner, P.A. Martoglio, G.P. Williams, Fourier-transform infrared microscopic analysis with synchrotron-radiation - the microscope optics and system performance, Rev. Sci. Instrum. 66 (1995) 1298–1302.

[61] G.L. Carr, Resolution limits for infrared microspectroscopy explored with synchrotron radiation, Rev. Sci. Instrum. 72 (2001) 1613–1619.

[62] M.C. Martin, P. Dumas, Materials sciences using synchrotron infrared light sources, Spectrosc. Prop. Inorg. Organomet. C: Tech. , Mater. Appl. 43 (2012) 141–165.

[63] H.Y.N. Holman, H.A. Bechtel, Z. Hao, M.C. Martin, Synchrotron IR spectromicroscopy: chemistry of living cells, Anal. Chem. 82 (2010) 8757–8765.

[64] L.M. Miller, P. Dumas, Chemical imaging of biological tissue with synchrotron infrared light, Biochim. Biophys. Acta 1758 (2006) 846–857.

[65] M.C. Martin, U. Schade, P. Lerch, P. Dumas, Recent applications and current trends in analytical chemistry using synchrotron-based Fourier-transform infrared microspectroscopy, Trac. Trends Anal. Chem. 29 (2010) 453–463.

[66] C. Petibois, M. Piccinini, M.C. Guidi, A. Marcelli, Facing the challenge of biosample imaging by FTIR with a synchrotron radiation source, J. Synchrotron Radiat. 17 (2010) 1–11.

[67] L. Bozec, A. Hammiche, M.J. Tobin, J.M. Chalmers, N.J. Everall, H.M. Pollock, Near-field photothermal Fourier transform infrared spectroscopy using synchrotron radiation, Meas. Sci. Technol. 13 (2002) 1217–1222.

[68] U. Schade, K. Holldack, P. Kuske, G. Wustefeld, H.W. Hubers, THz near-field imaging employing synchrotron radiation, Appl. Phys. Lett. 84 (2004) 1422–1424.

[69] U. Schade, K. Holldack, M.C. Martin, D. Fried, THz near-field imaging of biological tissues employing synchrotron radiation, in: Proceedings of the SPIE - The International Society for Optical Engineering 5725, 2005, pp. 46–52.

[70] Y. Ikemoto, T. Moriwaki, H. Okamura, T. Sasaki, N. Yoneyama, A. Taguchi, Y. Inouye, S. Kawata, T. Kinoshita, Broad band infrared near-field spectroscopy at fingerprint region using SPring-8, Infrared Phys. Technol. 51 (2008) 417–419.

[71] J. Puls, Photon-tunneling Spectroscopy with Synchrotron Infrared Radiation, Technical University of Applied Sciences, Wildau and Max-Born Institute, Berlin, 2007.

[72] Y. Ikemoto, M. Ishikawa, S. Nakashima, H. Okamura, Y. Haruyama, S. Matsui, T. Moriwaki, T. Kinoshita, Development of scattering near-field optical microspectroscopy apparatus using an infrared synchrotron radiation source, Optics Commun. 285 (2012) 2212–2217.

[73] P. Hermann, A. Hoehl, P. Patoka, F. Huth, E. Ruehl, G. Ulm, Near-field imaging and nano-Fourier-transform infrared spectroscopy using broadband synchrotron radiation, Optics Express 21 (2013) 2913–2919.

[74] P. Hermann, A. Hoehl, G. Ulrich, C. Fleischmann, A. Hermelink, B. Kaestner, P. Patoka, A. Hornemann, B. Beckhoff, E. Ruehl, G. Ulm, Characterization of semiconductor materials using synchrotron radiation-based near-field infrared microscopy and nano-FTIR spectroscopy, Optics Express 22 (2014) 17948–17958.

[75] J.D. Archangel, E. Tucker, E. Kinzel, E.A. Muller, H.A. Bechtel, M.C. Martin, M.B. Raschke, G. Boreman, Near- and far-field spectroscopic imaging investigation of resonant square-loop infrared metasurfaces, Optics Express 21 (2013) 17150–17160.

[76] H.A. Bechtel, E.A. Muller, R.L. Olmon, M.C. Martin, M.B. Raschke, Ultra-broadband infrared nanospectroscopic imaging, Proc. Natl. Acad. Sci. U. S. A 111 (2014) 7191–7196.

[77] P.M. Donaldson, C.S. Kelley, M.D. Frogley, J. Filik, K. Wehbe, G. Cinque, Broadband near-field infrared spectromicroscopy using photothermal probes and synchrotron radiation, Optics Express 24 (2016) 1852–1864.

[78] F. Peragut, J.B. Brubach, P. Roy, Y. De Wilde, Infrared near-field imaging and spectroscopy based on thermal or synchrotron radiation, Appl. Phys. Lett. 104 (2014) 251118.

[79] C. Sandt, S. Lefrancois, A. Dazzi, H. Bechtel, H. Yang, C. Prater, R. Brunetto, M. Kansiz, F. Borondics, FTIR Imaging and Spectroscopy with Six Decades Spatial Dynamic Range, Light, Energy and the Environment, Optical Society of America, Leipzig, 2016. FTu2E.3.

[80] I.D. Barcelos, A.R. Cadore, L.C. Campos, A. Malachias, K. Watanabe, T. Taniguchi, F.C.B. Maia, R. Freitas, C. Deneke, Graphene/h-BN plasmon-phonon coupling and plasmon delocalization observed by infrared nano-spectroscopy, Nanoscale 7 (2015) 11620–11625.

[81] B. Pollard, F.C.B. Maia, M.B. Raschke, R.O. Freitas, Infrared vibrational nano-spectroscopy by self-referenced interferometry, Nano Lett. 16 (2016) 55–61.

[82] R.O. Freitas, C. Deneke, F.C.B. Maia, H.G. Medeiros, T. Moreno, P. Dumas, Y. Petroff, H. Westfahl, Low-aberration beamline optics for synchrotron infrared nanospectroscopy, Optics Express 26 (2018) 11238–11249.

[83] P.M. Bridger, T.C. McGill, Observation of nanometer-scale optical property discrimination by use of a near-field scanning apertureless microscope, Optic Lett. 24 (1999) 1005–1007.

[84] M. Schnell, P.S. Carney, R. Hillenbrand, Synthetic optical holography for rapid nanoimaging, Nat. Commun. 5 (2014) 3499.

[85] T. Taubner, F. Keilmann, R. Hillenbrand, Nanoscale-resolved subsurface imaging by scattering-type near-field optical microscopy, Optics Express 13 (2005) 8893–8899.

[86] T. Taubner, F. Keilmann, R. Hillenbrand, Effect of tip modulation on image contrast in scattering-type near-field optical microscopy, J. Kor. Phys. Soc. 47 (2005) S213–S216.

[87] A.A. Govyadinov, S. Mastel, F. Golmar, A. Chuvilin, R.S. Carney, R. Hillenbrand, Recovery of permittivity and depth from near-field data as a step toward infrared nanotomography, ACS Nano 8 (2014) 6911–6921.

[88] S. Amarie, F. Keilmann, Broadband-infrared assessment of phonon resonance in scattering-type near-field microscopy, Phys. Rev. B 83 (2011), 045404.

[89] P. Hermann, B. Kastner, A. Hoehl, V. Kashcheyevs, P. Patoka, G. Ulrich, J. Feikes, M. Ries, T. Tydecks, B. Beckhoff, E. Ruhl, G. Ulm, Enhancing the sensitivity of nano-FTIR spectroscopy, Optics Express 25 (2017) 16574–16588.

[90] J.R. Birch, Dispersive fourier-transform spectroscopy, Mikrochim. Acta 3 (1987) 105–122.

[91] T.J. Parker, Dispersive fourier-transform spectroscopy, Contemp. Phys. 31 (1990) 335–353.

[92] M. Losurdo, K. Hingerl, Ellipsometry at the Nanoscale, Springer, Berlin, Heidelberg, 2013.

[93] S. Mastel, A.A. Govyadinov, T.V.A.G. de Oliveira, I. Amenabar, R. Hillenbrand, Nanoscale-resolved chemical identification of thin organic films using infrared near-field spectroscopy and standard Fourier transform infrared references, Appl. Phys. Lett. 106 (2015), 023113.

[94] R. Hillenbrand, F. Keilmann, Complex optical constants on a subwavelength scale, Phys. Rev. Lett. 85 (2000) 3029–3032.

[95] R. Hillenbrand, B. Knoll, F. Keilmann, Pure optical contrast in scattering-type scanning near-field microscopy, J. Microsc. Oxford 202 (2001) 77–83.

[96] A. Cvitkovic, N. Ocelic, R. Hillenbrand, Analytical model for quantitative prediction of material contrasts in scattering-type near-field optical microscopy, Optics Express 15 (2007) 8550–8565.

[97] A.S. McLeod, P. Kelly, M.D. Goldflam, Z. Gainsforth, A.J. Westphal, G. Dominguez, M.H. Thiemens, M.M. Fogler, D.N. Basov, Model for quantitative tip-enhanced spectroscopy and the extraction of nanoscale-resolved optical constants, Phys. Rev. B 90 (2014), 085136.

[98] B.Y. Jiang, L.M. Zhang, A.H.C. Neto, D.N. Basov, M.M. Fogler, Generalized spectral method for near-field optical microscopy, J. Appl. Phys. 119 (2016), 054305.

[99] J. Aizpurua, T. Taubner, F.J.G. de Abajo, M. Brehm, R. Hillenbrand, Substrate-enhanced infrared near-field spectroscopy, Optics Express 16 (2008) 1529–1545.

[100] Z. Fei, G.O. Andreev, W. Bao, L.M. Zhang, A.S. McLeod, C. Wang, M.K. Stewart, Z. Zhao, G. Dominguez, M. Thiemens, M.M. Fogler, M.J. Tauber, A.H. Castro-Neto, C.N. Lau, F. Keilmann, D.N. Basov, Infrared nanoscopy of Dirac plasmons at the graphene–SiO$_2$ interface, Nano Lett. 11 (2011) 4701–4705.

[101] M. Zhang, G.O. Andreev, Z. Fei, A.S. McLeod, G. Dominguez, M. Thiemens, A.H. Castro-Neto, D.N. Basov, M.M. Fogler, Near-field spectroscopy of silicon dioxide thin films, Phys. Rev. B 85 (2012), 075419.

[102] B. Hauer, A.P. Engelhardt, T. Taubner, Quasi-analytical model for scattering infrared near-field microscopy on layered systems, Optics Express 20 (2012) 13173–13188.

[103] X.Z. Chen, C.F.B. Lo, W. Zheng, H. Hu, Q. Dai, M.K. Liu, Rigorous numerical modeling of scattering-type scanning near-field optical microscopy and spectroscopy, Appl. Phys. Lett. 111 (2017) 223110.

[104] E.A. Muller, B. Pollard, H.A. Bechtel, P. van Blerkom, M.B. Raschke, Infrared vibrational nanocrystallography and nanoimaging, Sci. Adv. 2 (2016), e1601006.

[105] Z. Shi, H.A. Bechtel, S. Berweger, Y. Sun, B. Zeng, C. Jin, H. Chang, M.C. Martin, M.B. Raschke, F. Wang, Amplitude- and phase-resolved nanospectral imaging of phonon polaritons in hexagonal boron nitride, ACS Photonics 2 (2015) 790–796.

[106] E.A. Muller, B. Pollard, H.A. Bechtel, R. Adato, D. Etezadi, H. Altug, M.B. Raschke, Nanoimaging and control of molecular vibrations through electromagnetically induced scattering reaching the strong coupling regime, ACS Photonics 5 (2018) 3594–3600.

[107] I.D. Barcelos, A.R. Cadore, A.B. Alencar, F.C.B. Maia, E. Mania, R.F. Oliveira, C.C.B. Bufon, A. Malachias, R.O. Freitas, R.L. Moreira, H. Chacham, Infrared fingerprints of natural 2D talc and plasmon-phonon coupling in graphene-talc heterostructures, ACS Photonics 5 (2018) 1912–1918.

[108] Y.S. Lo, N.D. Huefner, W.S. Chan, P. Dryden, B. Hagenhoff, T.P. Beebe, Organic and inorganic contamination on commercial AFM cantilevers, Langmuir 15 (1999) 6522–6526.

[109] M. Suzuki, H. Nagasawa, Mollusk shell structures and their formation mechanism, Can. J. Zool. 91 (2013) 349–366.

[110] H.H. Adler, P.F. Kerr, Infrared study of aragonite and calcite, Am. Mineral. 47 (1962) 700–717.

[111] Z. Hao, H.A. Bechtel, T. Kneafsey, B. Gilbert, P.S. Nico, Cross-scale molecular analysis of chemical heterogeneity in shale rocks, Sci. Rep. 8 (2018) 2552.

[112] A. Barth, Infrared spectroscopy of proteins, Biochim. Biophys. Acta Bioenerg. 1767 (2007) 1073–1101.

[113] V. Stanic, F.C.B. Maia, R.D. Freitas, F.E. Montoro, K. Evans-Lutterodt, The chemical fingerprint of hair melanosomes by infrared nano-spectroscopy, Nanoscale 10 (2018) 14245–14253.

[114] G.C. Ajaezi, M. Eisele, F. Contu, S. Lal, A. Rangel-Pozzo, S. Mai, K.M. Gough, Near-field infrared nanospectroscopy and super-resolution fluorescence microscopy enable complementary nanoscale analyses of lymphocyte nuclei, Analyst 143 (2018) 5926–5934.

[115] G. Bakir, B.E. Girouard, R.W. Johns, C.R.J. Findlay, H.A. Bechtel, M. Eisele, S.G.W. Kaminskyj, T.E.S. Dahms, K.M. Gough, Ultrastructural and sins analysis of the cell wall integrity response of *aspergillus nidulans* to the absence of galactofuranose, Analyst 144 (2019) 928–934.

[116] R. Wiens, C.R. Findlay, S.G. Baldwin, L. Kreplak, J.M. Lee, S.P. Veres, K.M. Gough, High spatial resolution (1.1 μm and 20 nm) FTIR polarization contrast imaging reveals pre-rupture disorder in damaged tendon, Faraday Discuss 187 (2016) 555–573.

[117] R.W. Johns, H.A. Bechtel, E.L. Runnerstrom, A. Agrawal, S.D. Lounis, D.J. Milliron, Direct observation of narrow mid-infrared plasmon linewidths of single metal oxide nanocrystals, Nat. Commun. 7 (2016) 11583.

[118] E.L. Runnerstrom, A. Bergerud, A. Agrawal, R.W. Johns, C.J. Dahlman, A. Singh, S.M. Selbach, D.J. Milliron, Defect engineering in plasmonic metal oxide nanocrystals, Nano Lett. 16 (2016) 3390–3398.

[119] C.Y. Wu, W.J. Wolf, Y. Levartovsky, H.A. Bechtel, M.C. Martin, F.D. Toste, E. Gross, High-spatial-resolution mapping of catalytic reactions on single particles, Nature 541 (2017) 511–515.

[120] H.U. Yang, R.L. Olmon, K.S. Deryckx, X.G. Xu, H.A. Bechtel, Y. Xu, B.A. Lail, M.B. Raschke, Accessing the optical magnetic near-field through Babinet's principle, ACS Photonics 1 (2014) 894–899.

[121] M. Osawa, K. Ataka, K. Yoshii, Y. Nishikawa, Surface-enhanced infrared-spectroscopy - the origin of the absorption enhancement and band selection rule in the infrared-spectra of molecules adsorbed on fine metal particles, Appl. Spectrosc. 47 (1993) 1497–1502.

[122] R. Adato, A.A. Yanik, J.J. Amsden, D.L. Kaplan, F.G. Omenetto, M.K. Hong, S. Erramilli, H. Altug, Ultra-sensitive vibrational spectroscopy of protein monolayers with plasmonic nanoantenna arrays, Proc. Natl. Acad. Sci. U. S. A 106 (2009) 19227–19232.

[123] K.A. Smith, E.A. Nowadnick, S. Fan, O. Khatib, S.J. Lim, B. Gao, N.C. Harms, S.N. Neal, J.K. Kirkland, M.C. Martin, C.J. Won, M.B. Raschke, S.W. Cheong, C.J. Fennie, G.L. Carr, H.A. Bechtel, J.L. Musfeldt, Infrared nano-spectroscopy of ferroelastic domain walls in hybrid improper ferroelectric Ca$_3$Ti$_2$O$_7$, Nat. Commun. 10 (2019) 5235.

[124] S.N. Neal, H.-S. Kim, K.A. Smith, A.V. Haglund, D.G. Mandrus, H.A. Bechtel, G.L. Carr, K. Haule, D. Vanderbilt, J.L. Musfeldt, Near-field infrared spectroscopy of monolayer MnPS$_3$, Phys. Rev. B 100 (2019), 075428.

[125] X.W. Lu, O. Khatib, X.T. Du, J.H. Duan, W. Wei, X.L. Liu, H.A. Bechtel, F. D'Apuzzo, M.T. Yan, A. Buyanin, Q. Fu, J.N. Chen, M. Salmeron, J. Zeng, M.B. Raschke, P. Jiang, X.H. Bao, Nanoimaging of electronic heterogeneity in Bi$_2$Se$_3$ and Sb$_2$Te$_3$ nanocrystals, Adv. Electron. Mater. 4 (2018) 1700377.

[126] A. Politano, V.M. Silkin, I.A. Nechaev, M.S. Vitiello, L. Viti, Z.S. Aliev, M.B. Babanly, G. Chiarello, P.M. Echenique, E.V. Chulkov, Interplay of surface and Dirac plasmons in topological insulators: the case of Bi$_2$Se$_3$, Phys. Rev. Lett. 115 (2015) 216802.

[127] M.M. Qazilbash, M. Brehm, B.G. Chae, P.C. Ho, G.O. Andreev, B.J. Kim, S.J. Yun, A.V. Balatsky, M.B. Maple, F. Keilmann, H.T. Kim, D.N. Basov, Mott transition in VO$_2$ revealed by infrared spectroscopy and nano-imaging, Science 318 (2007) 1750–1753.

[128] J.M. Atkin, S. Berweger, E.K. Chavez, M.B. Raschke, J.B. Cao, W. Fan, J.Q. Wu, Strain and temperature dependence of the insulating phases of VO$_2$ near the metal-insulator transition, Phys. Rev. B 85 (2012), 020101(R).

[129] A.C. Jones, S. Berweger, J. Wei, D. Cobden, M.B. Raschke, Nano-optical investigations of the metal-insulator phase behavior of individual VO$_2$ microcrystals, Nano Lett. 10 (2010) 1574–1581.

[130] S.A. Dönges, O. Khatib, B.T. O'Callahan, J.M. Atkin, J.H. Park, D. Cobden, M.B. Raschke, Ultrafast nanoimaging of the photoinduced phase transition dynamics in VO$_2$, Nano Lett. 16 (2016) 3029–3035.

[131] P.N. Li, X.S. Yang, T.W.W. Mass, J. Hanss, M. Lewin, A.K.U. Michel, M. Wuttig, T. Taubner, Reversible optical switching of highly confined phonon-polaritons with an ultrathin phase-change material, Nat. Mater. 15 (2016) 870–875.

[132] A. Cavalleri, T. Dekorsy, H.H.W. Chong, J.C. Kieffer, R.W. Schoenlein, Evidence for a structurally-driven insulator-to-metal transition in VO$_2$: a view from the ultrafast timescale, Phys. Rev. B 70 (2004) 161102.

[133] A.J. Sternbach, J. Hinton, T. Slusar, A.S. McLeod, M.K. Liu, A. Frenzel, M. Wagner, R. Iraheta, F. Keilmann, A. Leitenstorfer, M. Fogler, H.T. Kim, R.D. Averitt, D.N. Basov, Artifact free time resolved near-field spectroscopy, Optics Express 25 (2017) 28589–28611.

[134] M.K. Liu, A.J. Sternbach, M. Wagner, T.V. Slusar, T. Kong, S.L. Bud'ko, S. Kittiwatanakul, M.M. Qazilbash, A. McLeod, Z. Fei, E. Abreu, J.D. Zhang, M. Goldflam, S.Y. Dai, G.X. Ni, J.W. Lu, H.A. Bechtel, M.C. Martin, M.B. Raschke, R.D. Averitt, S.A. Wolf, H.T. Kim, P.C. Canfield, D.N. Basov, Phase transition in bulk single crystals and thin films of VO$_2$ by nanoscale infrared spectroscopy and imaging, Phys. Rev. B 91 (2015) 245155.

[135] S.N.G. Corder, J.J. Jiang, X.Z. Chen, S. Kittiwatanakul, I.C. Tung, Y. Zhu, J.W. Zhang, H.A. Bechtel, M.C. Martin, G.L. Carr, J.W. Lu, S.A. Wolf, H.D. Wen, T.H. Tao, M.K. Liu, Controlling phase separation in vanadium dioxide thin films via substrate engineering, Phys. Rev. B 96 (2017) 161110.

[136] S.N.G. Corder, X.H. Chen, S.Q. Zhang, F.R. Hu, J.W. Zhang, Y.L. Luan, J.A. Logan, T. Ciavatti, H.A. Bechtel, M.C. Martin, M. Aronson, H.S. Suzuki, S. Kimura, T. Iizuka, Z. Fei, K. Imura, N.K. Sato, T.H. Tao, M.K. Liu, Near-field spectroscopic investigation of dual-band heavy fermion metamaterials, Nat. Commun. 8 (2017) 2262.

[137] J.W. Zhang, A.S. McLeod, Q. Han, X.Z. Chen, H.A. Bechtel, Z.Z. Yao, S.N.G. Corder, T. Ciavatti, T.H. Tao, M. Aronson, G.L. Carr, M.C. Martin, C. Sow, S. Yonezawa, F. Nakamura, I. Terasaki, D.N. Basov, A.J. Millis, Y. Maeno, M.K. Liu, Nano-resolved current-induced insulator-metal transition in the Mott insulator Ca$_2$RuO$_4$, Phys. Rev. X 9 (2019), 011032.

[138] R. Geick, C.H. Perry, G. Rupprech, Normal modes in hexagonal boron nitride, Phys. Rev. 146 (1966) 543–547.

[139] Z. Fei, A.S. Rodin, G.O. Andreev, W. Bao, A.S. McLeod, M. Wagner, L.M. Zhang, Z. Zhao, M. Thiemens, G. Dominguez, M.M. Fogler, A.H. Castro Neto, C.N. Lau, F. Keilmann, D.N. Basov, Gate-tuning of graphene plasmons revealed by

infrared nano-imaging, Nature 487 (2012) 82−85.

[140] J. Chen, M. Badioli, P. Alonso-Gonzalez, S. Thongrattanasiri, F. Huth, J. Osmond, M. Spasenovic, A. Centeno, A. Pesquera, P. Godignon, A. Zurutuza Elorza, N. Camara, F. Javier Garcia de Abajo, R. Hillenbrand, F.H.L. Koppens, Optical nano-imaging of gate-tunable graphene plasmons, Nature 487 (2012) 77−81.

[141] J.A. Gerber, S. Berweger, B.T. O'Callahan, M.B. Raschke, Phase-resolved surface plasmon interferometry of graphene, Phys. Rev. Lett. 113 (2014), 055502.

[142] A. Poddubny, I. Iorsh, P. Belov, Y. Kivshar, Hyperbolic metamaterials, Nat. Photon. 7 (2013) 948−957.

[143] A. Woessner, M.B. Lundeberg, Y. Gao, A. Principi, P. Alonso-Gonzaolez, M. Carrega, K. Watanabe, T. Taniguchi, G. Vignale, M. Polini, J. Hone, R. Hillenbrand, F.H.L. Koppens, Highly confined low-loss plasmons in graphene-boron nitride heterostructures, Nat. Mater. 14 (2015) 421−425.

[144] G.X. Ni, L. Wang, M.D. Goldflam, M. Wagner, Z. Fei, A.S. McLeod, M.K. Liu, F. Keilmann, B. Ozyilmaz, A.H.C. Neto, J. Hone, M.M. Fogler, D.N. Basov, Ultrafast optical switching of infrared plasmon polaritons in high-mobility graphene, Nat. Photon. 10 (2016) 244−247.

[145] F.C.B. Maia, B.T. O'Callahan, A.R. Cadore, I.D. Barcelos, L.C. Campos, K. Watanabe, T. Taniguchi, C. Deneke, A. Belyanin, M.B. Raschke, R.O. Freitas, Anisotropic flow control and gate modulation of hybrid phonon-polaritons, Nano Lett. 19 (2019) 708−715.

[146] J.M. Byrd, M.C. Martin, W.R. McKinney, D.V. Munson, H. Nishimura, D.S. Robin, F. Sannibale, R.D. Schlueter, W.G. Thur, J.Y. Jung, W. Wan, CIRCE: a dedicated storage ring for coherent THz synchrotron radiation, Infrared Phys. Technol. 45 (2004) 325−330.

[147] A. Jankowiak, G. Wüstefeld, Low-α operation of BESSY II and future plans for an alternating bunch length scheme BESSY-VSR, Synchrotron Radiat. News 26 (2013) 22−24.

[148] T. Moreno, Compact IR synchrotron beamline design, J. Synchrotron Radiat. 24 (2017) 386−391.

[149] T. Moreno, Optimized IR synchrotron beamline design, J. Synchrotron Radiat. 22 (2015) 1163−1169.

[150] T. Moreno, H. Westfahl, R.O. Freitas, Y. Petroff, P. Dumas, Optical layouts for large infrared beamline opening angles, J. Phys. Conf. 425 (2013) 142003.

[151] M.J. Booth, Adaptive optics in microscopy, Phil. Trans. Math. Phys. Eng. Sci. 365 (2007) 2829−2843.

[152] R.L. Olmon, M.B. Raschke, Antenna-load interactions at optical frequencies: impedance matching to quantum systems, Nanotechnology 24 (2013) 229501.

[153] F. Huth, A. Chuvilin, M. Schnell, I. Amenabar, R. Krutokhvostov, S. Lopatin, R. Hillenbrand, Resonant antenna probes for tip-enhanced infrared near-field microscopy, Nano Lett. 13 (2013) 1065−1072.

[154] S. Mastel, M.B. Lundeberg, P. Alonso-Gonzale, Y.D. Gao, K. Watanabe, T. Taniguchi, J. Hone, F.H.L. Koppen, A.Y. Nikitin, R. Hillenbrand, Terahertz nanofocusing with cantilevered terahertz-resonant antenna tips, Nano Lett. 17 (2017) 6526−6533.

[155] C. Maissen, S. Chen, E. Nikulina, A. Govyadinov, R. Hillenbrand, Probes for ultrasensitive THz nanoscopy, ACS Photonics 6 (2019) 1279−1288.

[156] S. Mastel, A.A. Goyyadinov, C. Maisseni, A. Chuvilin, A. Berger, R. Hillenbrand, Understanding the image contrast of material boundaries in IR nanoscopy reaching 5 nm spatial resolution, ACS Photonics 5 (2018) 3372−3378.

[157] B. Kaestner, F. Schmahling, A. Hornemann, G. Ulrich, A. Hoehl, M. Kruskopf, K. Pierz, M.B. Raschke, G. Wubbeler, C. Elster, Compressed sensing FTIR nano-spectroscopy and nano-imaging, Optics Express 26 (2018) 18115−18124.

[158] H.N. Lin, C.S. Liao, P. Wang, N. Kong, J.X. Cheng, Spectroscopic stimulated Raman scattering imaging of highly dynamic specimens through matrix completion, Light Sci. Appl. 7 (2018) 17179.

[159] S.C. Johnson, E.A. Muller, O. Khatib, E.A. Bonnin, A.C. Gagnon, M.B. Raschke, Infrared nanospectroscopic imaging in the rotating frame, Optica 6 (2019) 424−429.

[160] H.U. Yang, E. Hebestreit, E.E. Josberger, M.B. Raschke, A cryogenic scattering-type scanning near-field optical microscope, Rev. Sci. Instrum. 84 (2013), 023701.

[161] A.S. McLeod, E. van Heumen, J.G. Ramirez, S. Wang, T. Saerbeck, S. Guenon, M. Goldflam, L. Anderegg, P. Kelly, A. Mueller, M.K. Liu, I.K. Schuller, D.N. Basov, Nanotextured phase coexistence in the correlated insulator V_2O_3, Nat. Phys. 13 (2017) 80.

[162] O. Khatib, J.D. Wood, A.S. McLeod, M.D. Goldflam, M. Wagner, G.L. Damhorst, J.C. Koepke, G.P. Doidge, A. Rangarajan, R. Bashir, E. Pop, J.W. Lyding, M.H. Thiemens, F. Keilmann, D.N. Basov, Graphene-based platform for infrared near-field nanospectroscopy of water and biological materials in an aqueous environment, ACS Nano 9 (2015) 7968−7975.

[163] L.M. Meireles, I.D. Barcelos, G.A. Ferrari, P. Neves, R.O. Freitas, R.G. Lacerda, Synchrotron infrared nanospectroscopy on a graphene chip, Lab Chip 19 (2019) 3678−3684.

[164] Y.H. Lu, J.M. Larson, A. Baskin, X. Zhao, P.D. Ashby, D. Prendergast, H.A. Bechtel, R. Kostecki, M. Salmeron, Infrared nanospectroscopy at the graphene-electrolyte interface, Nano Lett. 19 (2019) 5388−5393.

[165] B.T. O'Callahan, K.-D. Park, I. Novikova, T. Jian, C.-L. Chen, E.A. Muller, P.Z. El-Khoury, M.B. Raschke, A.S. Lea, In liquid infrared scattering scanning near-field optical microscopy for chemical and biological nano-imaging, Nano Lett. 20 (2020) 4497−4504.

[166] M. Jin, F. Lu, M.A. Belkin, High-sensitivity infrared vibrational nano-spectroscopy in water, Light: Sci. Appl. 6 (2017), e17096.

[167] A.J. Huber, F. Keilmann, J. Wittborn, J. Aizpurua, R. Hillenbrand, Terahertz near-field nanoscopy of mobile carriers in single semiconductor nano-devices, Nano Lett. 8 (2008) 3766−3770.

[168] G.L. Carr, H.A. Bechtel, Design and development of a fast, far-infrared bolometer for near-field nanospectroscopy, WIRMS, in: 2019: 10th International Workshop on Infrared Microscopy and Spectroscopy with Accelerator Based Sources, Ubatuba, Brazil, 2019.

[169] J.M. Byrd, Z. Hao, M.C. Martin, D.S. Robin, F. Sannibale, R.W. Schoenlein, A.A. Zholents, M.S. Zolotorev, Terahertz coherent synchrotron radiation from femtosecond laser modulation of the electron beam at the Advanced Light Source, in: Proceedings of the 2005 Particle Accelerator Conference, 2005, pp. 3682−3684.